Numerical Simulation and Experimental Investigation of Salt-Diapirs

A Thesis

Submitted for the Degree of

MASTER OF SCIENCE (ENGINEERING)

by

DINESH KUMAR

ENGINEERING MECHANICS UNIT

JAWAHARLAL NEHRU CENTRE FOR ADVANCED

SCIENTIFIC RESEARCH

(A Deemed University)

Bangalore – 560 064

March, 2010

DECLARATION

I hereby declare that the matter embodied in the thesis entitled "**Numerical Simulation and Experimental Investigation of Salt-Diapirs**" is the result of investigations carried out by me at the Engineering Mechanics Unit, Jawaharlal Nehru Centre for Advanced Scientific Research, Bangalore, India under the supervision of Prof. K. R. Sreenivas and that it has not been submitted elsewhere for the award of any degree or diploma.

In keeping with the general practice in reporting scientific observations, due acknowledgement has been made whenever the work described is based on the findings of other investigators.

Dinesh Kumar

CERTIFICATE

I hereby certify that the matter embodied in this thesis entitled "**Numerical Simulation and Experimental Investigation of Salt-Diapirs**" has been carried out by Mr. Dinesh Kumar at the Engineering Mechanics Unit, Jawaharlal Nehru Centre for Advanced Scientific Research, Bangalore, India under my supervision and that it has not been submitted elsewhere for the award of any degree or diploma.

Prof K. R. Sreenivas

(Research Supervisor)

To my family & friends

Acknowledgements

I express my deepest gratitude to my research supervisor Prof. K. R. Sreenivas for introducing me to the challenging and interesting field of salt-diapirs. Because of his invaluable advice and guidance throughout my research work, I was able to make an organized effort. He provided me the essentials of freedom, funding, and facilities, allowing my work and education to truly flourish. I take this opportunity to convey my deep sense of respect to him for his valuable contribution in my academic career.

I thank Prof. Rama Govindrajan and Dr. Ganesh Subramaniam for providing me with valuable suggestions. I thank all my teachers at JNC and IISc for providing guidance and support. I would like to thank computer lab staff and head Dr. Meheboob Alam for providing excellent computational facilities for my work.

Next there are all friends I've made, the list is too long to mention but their friendship, cooperation, company and help to make my stay at JNCASR a happy one. I thank all of my batch mates at JNCASR. I would like to thank Dr. Vishvanath, Sumesh and Ratul for correcting my thesis and comments.

I thank to all members of my undergraduate hostel wing for giving me everything that a family can give, without actually being one.

Finally, I convey my regards to my family for their love and support.

Abstract

The main focus of this thesis has been to understand the dynamics of salt-diapiric structures and the role of various parameters that govern the diapir structures with the help of Rayleigh-Taylor fluid instability. Rayleigh-Taylor instability occurs in the presence of two fluid layers with different viscosity and density.

In this work, we present results from 2-D numerical simulations and laboratory model experiments to explain characteristics of salt-diapirs and its dependence on governing parameters. We in this study considered a two-layer system that contains heavier layer fluid lying over lighter fluid layer and these layers are of different thickness. For simulating this system, a code based on finite volume discretization and semi implicit method for pressure linked equations revised (SIMPLER) algorithm is used. Initial condition is a step-profile for concentration (density) with heavier fluid (representing sedimentary soil layer) laying-over lighter fluid layer (representing evaporative mineral layer) and is allowed to evolve in time due to diffusion and convection. Resulting Rayleigh-Taylor fluid instability helps in understanding characteristics of salt-diapirs on various governing parameters.

We have also done experiments with similar configuration in a tank in which an initial step change in density across an interface (stable) is established using two layers of fluids with different densities and high viscosities. We used CMC (Carboxy Methyl Cellulose) to vary the viscosity of the water and sugar to increase the density. The unstable density stratification was obtained by inverting the tank. Experiments are done with different density difference and layer thickness ratios. Experimental results provide quantitative verification of the simulations.

Nomenclature

Symbols : **Description**

g : acceleration due to gravity (m/sec^2)
H : height of the cell
E_k : non dimensional kinetic energy
$E_{k,max}$: maximum non dimensional kinetic energy
Pr : Prandtl number=v/k_T
R_{acr} : critical Rayleigh number
R_{aT} : thermal Rayleigh number
R_{as} : salinity Rayleigh number
k_T : thermal molecular diffusion coefficient
ks : saline molecular diffusion
T_0 : reference temperature
ΔT : temperature difference across the interface
S : salinity (% of mass fraction)
S_0 : initial salinity
Sc : Schmidt number
ΔS : salinity difference = S-S_0
T : temperature
u : non dimensional horizontal velocity
U : dimensional horizontal velocity (m/sec)
v : non dimensional vertical velocity
V : dimensional vertical velocity (m/sec)
t : time in sec
t^* : non dimensional time
t_o : onset time
x : non dimensional horizontal coordinate
X : dimensional horizontal coordinate (m)
Y : non dimensional vertical coordinate
y : dimensional vertical coordinate (m)
TR : layer thickness ratio

Greek symbols

β_S : salinity expansion coefficient ($\%^{-1}$)
β_T : temperature expansion coefficient ($\%C^{-1}$)
$\beta_s \Delta S$: dimensionless density step due to slower diffusing component

$\beta_T \Delta T$: dimensionless density step due faster diffusing component

v : kinematic viscosity
μ : dynamic viscosity
ρ : density($kg/m3$)
ρ_o : reference density ($kg/m3$)
$\Delta\rho$: density anomaly across the interface ($kg/m3$)

Abbreviations

CMC : sodium carboxy methyl cellulose
K.E : kinetic energy
P.E : potential energy

List of Figures

1.1 (a) Salt Dome on Melville Island, Northern Canada (b) Underwater Salt diapirs, Gulf of Mexico (c) Seismic reflection image of the underground diapiric structure 1
1.2 Cross section of the earth 3
1.3 Density inversion in deep earth crust 4
1.4 Evolution of a salt diaper 7
1.5 Seismic section of a saltdome 8
1.6 A schematic illustrating the Rayleigh Taylor 10
1.7 Zagros chain, Iran (Dark regions are associated with salt domes) 12
2.1 Schematic diagram of domain 16
2.2 Schematic of the computational domain with initial and boundary conditions 20
2.3 Contour plot of concentration, Effect of layer thickness ratios (TR) for constant Gr (40000) and Sc (1000). 26
2.4 Contour plot of concentration, Effect of layer thickness ratios (TR) for constant Gr (90000) and Sc (1000). 26
2.5 Contour plot of concentration, Effect of small variation of Gr number for constant Sc (1000) and layer thickness ratio (TR =7/13). 30
2.6 Contour plot of concentration, Effect of large variation in Gr number for constant Sc (1000) and layer thickness ratio (TR = 1/19). 32
2.7 Contour plot of concentration, Effect of variation in Sc number for constant Gr 104 (a,b,c,d) & 109 (A,B,C,D) and layer thickness ratio (TR = 1/19) 34
3.1 Schematic diagram showing the experimental setup 36
3.2 (a) Vacuum Chamber (b) Vacuum pump 37
3.3 Traverse and laser arrangement 39
34 (a) Laser (b) Schematic of laser and optic arrangement 39
3.5 Viscosity v/s shear rate for a general fluid 41
3.6 Viscosity v/s concentration of CMC [Vivek N.P. et al. 2009] 43
3.7 Extended plot of viscosity v/s concentration of CMC 43
3.8 A schematic of flow visualization process 45
3.9 Evolution of salt-diapir like structures in laboratory 49
3.10 Time sequence of six vertical planes showing the evolution of concentration field in six planes 50
3.11 Raw images of Diapiric structures (a,b,c) and corresponding Matlab processed binary images(d,e,f). 50
3.12 3D diapiric structure for TR = 1:4 51
3.13: Location and thickness of diapiric structures in the experimental tank 52
3.14 Height of diapiric structures as a function of time 53
3.15: Diapiric structure formation for layer thickness ratio 2/3. Six columns are six different vertical cross-section of the experimental tank 54

3.16 3D image for the case of TR = 2/3. 54
3.17 Diapiric structure formations for layer thickness ratio 1/9 55
3.18 Evolution of diapiric structures with time for 3.5%CMC solution 55
3.19 3D diapiric structure of 3.5% CMC case 56
3.20 Time evolution of diapiric structures for 3% CMC solution 56
3.21 Experiments with less viscous fluid (2.5% CMC ~ 5.0X105 mPa-s) 57
4.1 Variation of average spacing between diapirs with Gr number at constant Sc number (1000) and layer thickness ratio (1/19) 60
4.2 Variation of average thickness of diapirs with Gr number at constant Sc number (1000) and layer thickness ratio (1/19) 61
4.3 Variation of spacing between diapiric structures with layer thickness ratios for Gr number 40000 63
4.4 Variation of average thickness of diapiric structures with layer thickness ratios for Gr number 40000 63
4.5 Evolution of kinetic energy at Sc = 10000 and Tr=1/19 65
4.6 Evolution of kinetic energy at Sc = 1000 and Gr = 10^5 66
4.7 Effect of Sc number [Gr=10^4 and TR = 1/19] 67
4.8 Variation of average spacing with layer thickness ratio 68
4.9 Variation of average thickness with layer thickness ratio 69
4.10 Spacing and thickness of diapiric structures extracted from our study for Ra ≈10^7 71

Tables

1.1: Properties of typical salt and sediment rocks 6

3.1: A list of all the experiments and their parameters 48

3.2: Location of diapiric structures and evolution of height with time 52

4.1: Variation in number of structures, average spacing and average thickness with Gr number 59

4.2: Number of structures, average spacing and thickness with Gr number 62

4.4: Variation of the diapirs parameters with layer thickness ratio 68

Contents

Acknowledgements **I**
Abstract **III**
Nomenclature **V**
List of Figures **IX**
List of Tables **XI**

1 Introduction **1**
1.1 Background 1
1.2 Salt movement. 2
1.3 Traps associated with salt domes. 6
1.4 Identification od salt structures 6
1.5 Evolution of salt diapirs. 7
1.6 Rayleigh Taylor instability 9
1.7 Previous theory and investigation. 11
1.8 Motivation. 12
1.9 Thesis overview. 13

2 Numerical Modeling and Simulation **15**
2.1 Numerical model 15
2.1.1 Mathematical formulation 15
2.1.2 Dimensionless equations. 17
2.1.3 Non-dimensional parameters 19
2.1.4 Initial and boundary conditions 19
2.1.5 Velocity boundary conditions 19
2.1.6 Temperature and concentration boundary conditions 20
2.2 Numerical methodology. 20
2.2.1 ADI method 21
2.2.2 SIMPLER algorithm. 23
2.3 Results and simulations. 25
2.3.1 Layer thickness effect on diapiric structures 25
2.3.2 Gr number effect on diapiric structures. 28
2.3.3 Sc number effect on diapiric structures. 33

3 Experimental Setup and Measurements **35**
3.1 Experimental setup. 35
3.2 Bubble removing mechanics and setup 36

3.3 Setup to accelerate outfloe from vacuum chamber……38
3.4 Traverse mechanics……..….38
3.5 laser and optics……..39
3.6 Viscosity enhancement……..39
3.7 Solution preparation……...41
3.8 Viscosity measurements…… ……....42
3.9 Flow visualization……....44
3.10 Experimental procedure……....44
3.11 Experimental details…….…..…46
3.12 Convective diapiric structures and analysis ……..……....47
3.12.1 Layer thickness effect on diapirs like structures……48
(a) Layer thickness ratio TR = 1:4…….....49
(b) Layer thickness ratio TR = 2:3 ……..…...53
(c) Layer thickness ratio TR = 1:9……..54
3.12.2 Viscosity effect on diapiric structures…. ……55
(a) 3.5 % CMC solution …….……55
(b) 3 % CMC solution…….……56
(c) 2.5 % CMC solution…….……..…57

4 Results and Analysis **58**
4.1 Simulations results……..58
4.1.1 Effect on average spacing and thickness……58
(a) Effect of Gr number ……58
(b) Effect of thickness ratio (TR)…….……...61
(c) Effecnt of sc number …….……....64
4.1.2 Effect on kinetic energy …….……...64
(a) Effect of Gr number…….……64
(b) Effect of layer thickness ratio…….…….65
(c) Effect of Sc number…….…….....66
4.2 Experimental results and comparison with simulations…….…….…….67
4.2.1 Effect of layer thickness ratio…….…….…….67
4.3 Dynamics of salt-diapirs…….…….70
4.4 Predicting the spacing and width of salt-diapirs…….…70

.
5 conclusion and Future Outlook **73**

Chapter -1

Introduction

1.1 Background

The research work reported in this thesis is aimed towards understanding the basic characteristics of Rayleigh-Taylor instability and its role in formation of geological structures 'salt-diapirs' (also called salt domes). Salt diapers (figure 1) are dome shaped geological structures formed by intrusion of evaporative mineral-deposits rising through sediment. Pressure in the earth's crust have caused normally bedded salt deposits to flow laterally and upward plastically, first bulging and then in many places rupturing the overlying sediments**.** Salt refers to all rocks composed mostly of evaporated minerals.

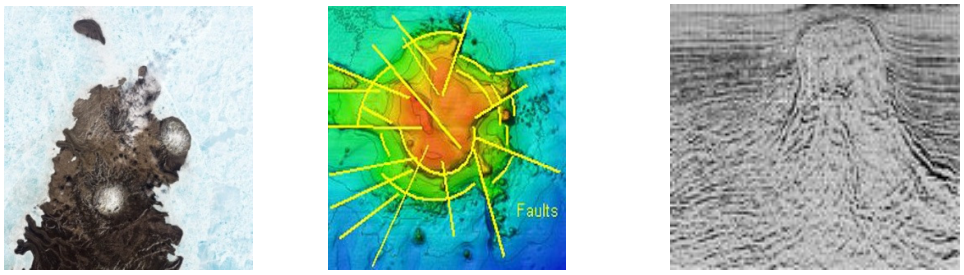

(a) **(b)** **(c)**

Figure 1.1: (a) Salt Dome on Melville Island, Northern Canada (Satellite Image) [Ref. web1] (b) Underwater Salt diapirs, Gulf of Mexico [Ref. web2] (c) Seismic reflection image of the underground diapiric structure [Ref. web3]

The characteristic length scales of these structures are the diameter (~1000m) and the spacing between them (~10km). Rising-velocity is another important factor. Their shape may vary from circular to broadly elliptical, bell-shaped or mushroom-like. The movement of thick salt beds into overlying sediment layers has created hydrocarbon reservoirs around the world.

Reservoirs associated with these salt structures can be found in Germany, Gulf of Mexico, Middle East, Southern Russia, Southern France, Utah and the Atlantic Seaboard of Canada.

In this work we study the dependence characteristics of salt-diapirs on governing parameters like ratio between heights of mineral deposited and overlaying sedimentary layer, viscosity and the density difference between these two layers. In nature, because of very high viscosity, the emplacement of salt layer into soil-layer happens over geological time scales. Salt structures are most often found in active rifts or along previously rifted continental margins. Beds of evaporates are commonly deposited in such areas during the early ocean phase of continental rifting.

It is common to model creeping motion of the solid earth by hydrodynamic models. This is possible because solid earth exhibits a fluid behavior over geological time scales [Turcotte, 1983]. Further more, because of the uncertainties involved in the spatial variations in temperature, pressure and composition, and their predominant effect on viscosity, it is safe to assume Newtonian rheology for modeling mantle and crustal dynamics, which are extremely slow moving, highly viscous, complex fluid flows [King, 1995; Haskel, 1937 and Balachandar et. al., 1992].

1.2 Salt movement

It has been well accepted that density inversion in the earth-crust is responsible for the formation of salt-diapirs [see Hudec, M. R., and Jackson, 2007]. Density inversions within sedimentary sequences provide an opportunity for underlying sediments to deform those above them. These inversions can have a significant effect on the evolution of geological structures within a planetary crust. Rayleigh-Taylor instabilities at the interface between a low density mineral layer and the denser sedimentary layer above may lead to the formation

of diapiric upwelling. This is typically seen in sequences which contain evaporates.

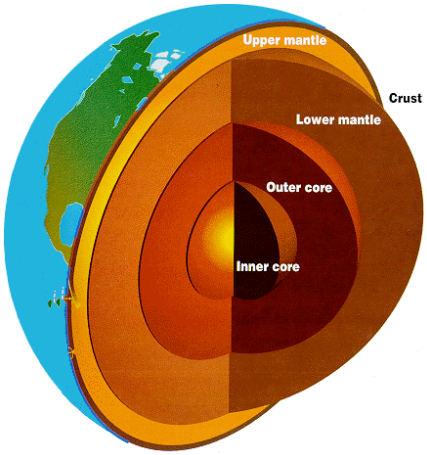

Figure 1.2: Cross section of the earth [Ref. web4]

The average radius of the earth is about 6370 km. Starting from the surface to 10 km depth is called the earth-crust. The lithosphere extends from 10 km to a depth of 100 km. The region from 100 km to 660 km is referred to as the upper mantle. The lower mantle extends from 660 km till the Core-Mantle Boundary at a depth of about 2800 km. The outer core extends from 2800 km to a depth of 5000 km [see Geoffrey Davies (1999)].The inner solid core exists beneath the outer core. Figure 1.2 shows the cross-section of the earth crust.

Salt's low density and flowability in the earth crust make it particularly susceptible to movement at shallow depths. Halite attains a density of 2.2 gm/cm^3 within a few meters of burial. It then changes only slightly with further burial. During deposition, density of the overlying sediment is less than that of the halite unit but increases with depth as it compacts and dewaters. By depths of 0.5 to 0.9 km (2000 to 6000 feet) it exceeds that of the underlying salt, making underlying salt layer buoyant. Salt tends to decrease in density with depth. Salt's volume increases with increasing temperature, faster than it contracts from the increase in overburden pressure. The low-rheidity of salt is the ease with which salt flows as a viscous solid. Salt flows under burial conditions where the surrounding sediment is still undeformed. The mineral halite has an unusual behavior, as it can become slightly less dense with deep burial. At a depth of 5 km (17000ft) under a geotherm of 30°C/km halite expands 2% due to

heat and contracts 0.5% due to pressure. Salt layers become less dense with burial in contrast to all other sedimentary minerals [see Jackson and Seni (1984)] as shown in figure 1.3. The salt flow should be induced thermally at depths of more than 1.5 km (5000 ft) under such a geothermal regime. The viscosity of Gulf of Mexico salt is 10^{14} to 10^{17} Pa-s, depending on moisture content and temperature. The viscosity of the overburden is about 10^{21} Pa-s.

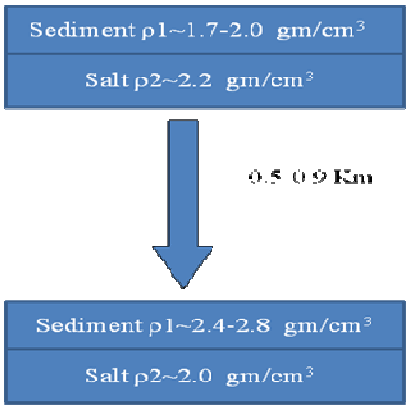

Figure 1.3: Density inversion in deep earth crust

Temperature, density contrast, salt thickness, viscosity, and salt moisture content control the salt-layer fluidity. Salt can move only when it has been triggered. The triggering mechanism can operate at shallow depth (~900m) or at much greater depths. Shallow triggers are usually important in initiating salt flow during or soon after deposition of the salt unit. Deeper triggers can initiate salt flow even after the unit has been buried for millions of years. Deep salt flow is triggered by tensional or compressional stresses. The flow can also be triggered by burial of salt to the critical depth where it becomes plastic [John Warren, 2006].

Triggers are commonly tied to some sort of irregularity in the basin. These irregularities are located in the mother salt bed (source layer) or in the overburden. Irregularities in the salt bed include lateral changes in thickness, density, viscosity or temperature and are often related to geological changes in the salt unit [John Warren, 2006].

From available field data, it is difficult to state the initial layer thicknesses of soil and overlying sediment. Present day data has been collected using seismic reflection technique which indicates the current configuration of soil and sediments. Age and other properties of some of known salt diapirs have to be estimated. Some of these estimations have been given below.

Sverdrup basin in Canada, the density of overlying sediment is 2900 – 3000 kg/m^3 and of soil is 2200 – 2900 kg/m^3. Sverdrup deformation is estimated to have started between 1050 and 950 Ma. In early 940–850 Ma, evaporitic diapirs enlarged (Jackson, 2003 and 2006). Full thickness of this diapir is unknown because of dismemberment and missing sections and only up to 1600 m thickness is exposed (Francois, 1991 — referred in Jackson 2003)

Average vertical growth rates of diapirs is about few-mm/yr during initial stages of growth and in diapirs subjected to tectonic compression The development of diapirs is often not steady-state, however, and many diapirs experience multiple surges in growth (Koyi, 2001 and Jackson & Talbot, 1991). The width of diapirs in the Mediterranean is typically 2 to 4 km. At the Southern Grand Bank margin of the water depth is 3 km and the sedimentary thickness is 4 to 8 km. Three known diapirs are deeply buried below 600 m to 4,000 m of sediments (Guy Pautot, 1970).

Weinberger et. al. (2006) did mechanical modeling of Dead Sea Basin and determined viscosity of Sedom rock salt between 2 and 3X10^{18} Pa.s. They also showed that the maximum uplift rates of Mount Sedom are 8.3 and 5.5 mm/yr for its northern and southern parts, respectively. They also predicted that Sedom rock salt began to migrate laterally and upward at about 2.2 Ma (million years ago). The Holocene rate of rise of the Sedom diapir has been estimated by several approaches to vary between 5 and 11 mm/yr [Weinberger et al., 2006, and references therein]. The overburden sediment is about 1,700m to 3,700 m thick

of Mount Sedom. On the basis of data available the properties of diapiric rocks have been tabulated below:

Density of salt layer	2200 to 2400 kg/m^3
Density of sediment layer	2400 to 2900 kg/m^3
Thickness of salt and sediment layer	1 to 8 km
Viscosity of salt / sediment layer	2 to 3X10^{18} Pa.s
Age of diapirs	600 to 900 Millions year
Growth rate	2 to 8 mm/year

Table1.1: Properties of typical salt and sediment rocks

From the Table, typical density difference is about 400kg/m3, layer viscosity is about 10^{18} Pa.s and assuming mass diffusivity to be around 10^{-10} m^2/s, typical Rayleigh number would be about 10^6, hence simulations are done around this value.

1.3 Traps associated with salt domes

If salt layers are under enough pressure and heat, they will slowly flow like a glacier that slowly but continually moves downhill. Unlike glaciers, salt which is buried kilometers below the surface of the Earth can move upward until it breaks through to the Earth's surface. In the process of breaking the earth's surface, it has to push aside many layers of rocks in its path. This will create traps and cavities. Because of the abundance and variety of traps created by salt movement, hydrocarbons are commonly found around salt domes.

1.4 Identification of salt structures:

Seismic profiling is commonly used to define the subsurface configuration of salt domes. The subsurface geometry of a salt-dome is usually obtained by shooting seismic lines radially over the feature (fan shooting). A salt mass is relatively homogeneous with indefinite bedding planes so the reflections from within the salt are scarce. Seismic reflections-occur at

boundaries where there are changes in acoustic impedance (the velocity of salt is higher than that of a normal sand-shale sequence).

Gravity and magnetic data, when integrated with the detailed seismic results, can be used to discriminate between alternative and equally possible seismic interpretations. This multi-disciplinary integration can also provide valuable information where seismic data alone may be difficult to interpret. In addition, gravity and magnetic data can be used to improve velocity models, where velocities derived entirely from seismic data are typically interpolated over large distances.

1.5 Evolution of a salt diapir

Salt diapirs can evolve from a mass of salt to a diapir and then to a smaller detached sheet (figure 1.4). Salt is less dense than other sediments so it tends to flow upward, piercing the overlying material and in some cases, forming traps in which hydrocarbons can accumulate. Salt refers to all rocks composed mostly of evaporite minerals, excluding most carbonates. Rock salt is a crystalline collection of the mineral halite (NaCl). Salt is mechanically weak and flows like a fluid, even under geologically rapid strain rates. Figure 1.5 shows seismic section of a salt-diapir with the lines representing true sides of salt-dome. Salt's fluid rheology and incompressibility make it naturally unstable under a wide range of geologic conditions.

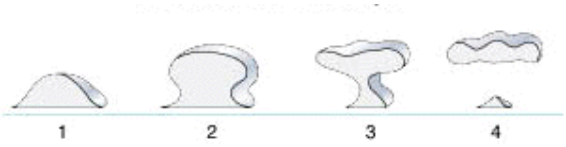

Figure 1.4: Evolution of a salt diapir [Ref. web5].

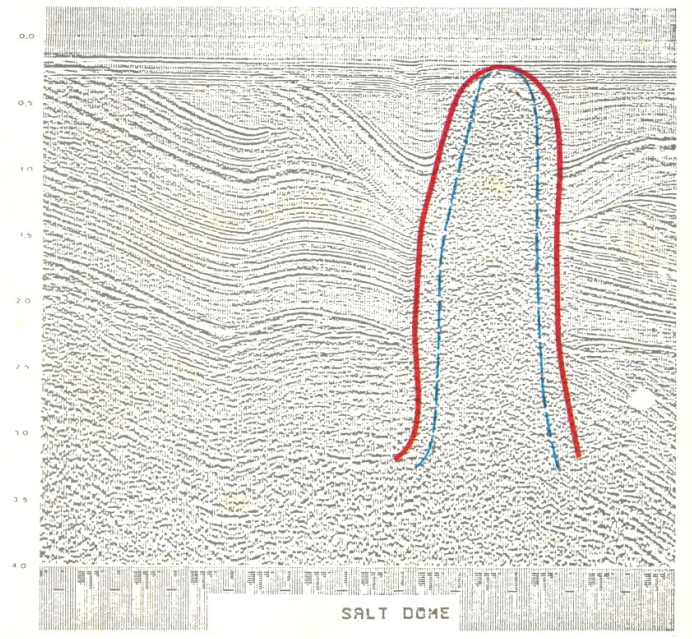

Figure 1.5: Seismic section of a saltdome with the bold (continuous) line representing the beginning of abrupt termination of continuous reflection events. The dashed line represents the true sides of the salt mass which is within the 'no reflection' or disturbed zone [Ref. Meisner et al. 2009].

Rock salt is almost incompressible and maintains its relatively low density under high pressures. After deposition of the salt in evaporite basins and subsequent burial by increasingly denser sediment, a density inversion can occur and this may lead to the formation of salt domes. The large economical interests, associated with hydrocarbon trapping and long term storage of radioactive waste and energy reserves, have lead to an extensive study of the dynamics of salt dome formation using analytical methods [see Hunsche (1977) and Ramberg (1981)], experimental approaches [Whitehead & Luther (1975), Talbot (1977) and Jackson et al. (1990)] and numerical modeling [Berner et al. (1972), Woidt (1978) and Schmeling (1987)].

In both the analytical and numerical approaches, the mathematical model used has been Rayleigh-Taylor instability - a gravitational instability of a layer of heavy fluid overlying a lighter one [Chandrasekhar, 1961]. In 1960, Trusheim described evolutionary stages of salt movements. He interpreted such evolutionary stages as typical stages of buoyant Rayleigh-Taylor instability. After compiling data from more than 200 salt structures in northern Germany, Trusheim summarized their main characteristics. Trusheim further developed his conceptual model for interpretation of the growth of salt structures. The conventional wisdom in his article was that the genesis and growth of salt diapirs were the results of Rayleigh-Taylor instabilities. Prior to Trusheim's article, Nettleton (1934) used model-experiments to investigate the progressive evolution of these structures.

1.6 Rayleigh Taylor instability

Spontaneous mixing of fluids at unstably stratified interfaces occurs in a wide variety of atmospheric, oceanic, geophysical and astrophysical flows. In the presence of gravity, the fluid layer rises because of a buoyancy force when it becomes lighter than the surrounding fluid. Once the motion starts, the potential energy of the fluid is converted to kinetic energy in the form of buoyant motion and is finally dissipated. The source of the buoyancy force is a density difference that can be created either by thermal heating or by concentration differences (compositional buoyancy). The Rayleigh-Taylor instability is one of the hydrodynamic instabilities that are easiest to observe. The Rayleigh-Taylor instability is of a fingering type on an interface between two fluids of different densities. It occurs when a light fluid is accelerated into a heavy fluid and is a fundamental fluid-mixing mechanism. It is a dynamic process by which fluids seek to reduce their combined potential energy.

In 1880, Lord Rayleigh first derived the interfacial motion that occurs when a heavy fluid is supported by a lighter one. He considered the idealized case of two incompressible

immiscible fluids in a constant gravitational field. In 1950, Sir G.I. Taylor recognized that Rayleigh's interfacial instability also occurs for accelerations other than gravity.

Rayleigh-Taylor (RT) instability results due the unstable equilibrium of two fluid layers with a heavier fluid on top of a lighter fluid. A schematic is shown in figure 1.6. The two fluids in this configuration overturn as the system seeks to minimize its potential energy. The main

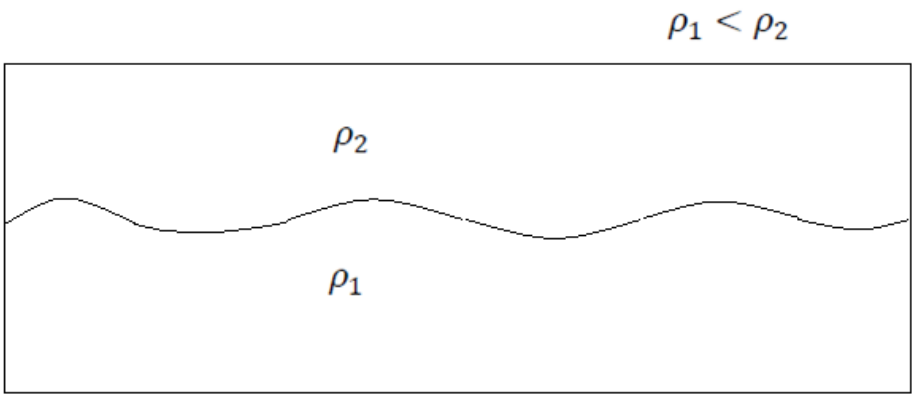

Figure 1.6: A schematic illustrating the Rayleigh Taylor instability

focus of RT studies is to study the mixing and turbulence that results as a consequence of the overturning fluids. The RT instability is a very well studied phenomenon in literature. For example Young et al 2001 have carried out a numerical investigation of the RT instability of miscible fluids. The RT instability is relevant in fields like astrophysics, geophysics and in technological applications like nuclear fusion reactors.

Understanding the rate of mixing caused by Rayleigh-Taylor instabilities is important to a wide variety of applications, including inertial confinement fusion, nuclear weapons explosions, supernova explosions, in air bubble formation, blood of deep sea divers and many industrial processes.

1.7 Previous theory and investigation

Understanding the dynamics of salt diapirs formation, being an important problem in geophysics and petroleum industry has received a lot of attention. Even beyond its importance to hydrocarbon geology, advances in salt tectonics are shedding light on a much wider range of problems. For example, advances in the understanding of diapiric processes are influencing work in shale tectonics and in extraterrestrial geology [e.g., Schenk and Jackson (1993), Pappalardo and Barr (2004)]. Several reviews have been written on different aspect of salt diapirs.

From 1901-1916, keen interest in domes was shown as a result of the economic impact of giant salt dome oil fields. From 1916-1924, there was widespread acceptance of salt-flow principles to explain dome formation.

European scientists first advanced the idea that salt could flow in a plastic or semi-plastic state under natural conditions and form structures. As other basic theories, the salt-flow concept has also been explained in several different ways. Two principal schools of thought include (1) salt structures produced by lateral or tangential compression (2) salt structures produced by gravitational non-equilibrium resulting from density differences between salt and surrounding sediments. Nettleton (1934) developed a theory, known as the "fluid mechanical concept". This is basically the same theory that is widely accepted by American geologists today. Nettleton recognized that the prime motive force was the density contrast between salt (specific gravity 2.2) and sediments (specific gravity ranging from 1.7-2.0 at the surface to 2.4-2.8 at depth). He conducted experiments on different materials to simulate model domes and concluded that the final form of a dome depends largely on the following factors:

(1) Initial configuration which localized the dome

(2) Thickness of the salt layer

(3) Strength or viscosity of the overlying rocks

(4) Strength or viscosity of the salt

1.8 Motivation

Most of the work done in this field is analytical and empirical. Research areas have been touched in these studies include mathematical modeling of salt structures, shaping of salt diapirs, determining the geometry, age prediction, mechanical properties and behavior of these salt rocks. It has been observed that these salt diapir structures are always found in the form of clusters or in a pattern.

A number of evidence indicates that the pattern or geometric arrangement of these salt structures is not by coincidence and that some domes, especially clusters of domes are related in their history of development. Figure 1.7 shows a satellite image of a chain of salt diapirs in the form of a cluster, found in Iran. This chain of salt diapirs is called Zagros chain.

Figure 1.7: Zagros chain, Iran (Dark regions are associated with salt domes) [Ref. web6]

In summary, the literature review indicates that most of the earlier work was to study the diapiric basins, related to the study of their properties like shape, density, viscosity, stress and

age through two dimensional numerical simulations [Woidt 1978, Romer and Neugebauer, 1991; Van Keken et al., 1993; Poliakov et al. 1993 and Daudre´ and Cloetingh, 1994], lab experiments [Mukherji et. al.,, 2009)], field experiments and analytical studies modeling formation of salt-diapir as Rayleigh-Taylor instability. Seismic methods have been used for field experiments [Meisner et al. 2009]. Rayleigh Taylor instability and Newtonian viscous fluid models have been used in experiments, numerical-simulations and analytical studies [Naimark and Ismail-Zadeh, 1989; Conrad and Molnar, 1997; Ismail-Zadeh et al., 2001 & 2002]. To the best of our knowledge no study has been done for diapiric cluster formation and its dependency on parameters like layer thickness ratio, viscosity and density contrast. Mukherji et. al., (2009) have modeled deformation of salt-layer in the Hormuz- and the Namakdan salt diapirs at the Persian Gulf by Newtonian viscous fluid to get velocity profiles and to estimate viscosity of the salt layer.

1.9 Thesis overview

In the present study, we have focused on the formation of salt-diapirs; that is to study the variation in spacing between diapirs and diameter of diapirs with the variation in thicknesses of two layers, density difference and viscosity of layers in the salt diapiric system. From experiments and simulations we predict how spacing between diapirs, their diameter and pattern of salt structures vary with layer thickness ratio, viscosity and density difference of salt and sediments.

We have used 2D code, based on finite volume method with SIMPLER algorithm for simulations presented in the thesis. This code has been validated for single diffusive and double diffusive convection with experimental results, have been used to study double diffusive convection, code validation and related results are available in Sreenivas K. R. et. al. 2009. Experiments are done using very high viscosity, CMC-water solution of different densities. Sugar has been used to increase the density of the solution. Effect of variation in

layer thickness ratio, density difference and viscosity on salt-dipiric system has been studied through experiments. Analogue to density difference and viscosity variation, non dimensional parameters; Gr number and Sc number have been varied in order to simulate salt diapir numerically. Some of the simulation results have been matched with experiments for same Rayleigh number.

In this thesis, we represent formulation of the two dimensional numerical model to simulate Rayleigh-Taylor instabilities followed by laboratory experiments using Newtonian fluid model. This thesis is organized as follows: The mathematical modeling and simulation details are given in Chapter 2 and Chapter 3 describes the experimental setup and procedures. Chapter 4 describes the results and analysis of our work. We present conclusions from our study in Chapter 5.

Chapter 2

Numerical Modeling and Simulation

In this chapter we will describe the numerical modeling of Rayleigh Taylor instability. We describe the two dimensional equations, non dimensional governing parameters and the boundary conditions, used to solve the Rayleigh Taylor instabilities. Using two-dimensional model for the study of RT instability is justified as two-dimensional modes are found to be fastest growing modes in this scenario [Refer Turner, 1971]. Two dimensional analysis have been extensively used to predict critical Rayleigh number for the onset of convection and dominant wavelength [Banis and Gill, 1966; Nield, 1967] in the double diffusive convection. These analysis have been extended to cover general boundary conditions by Walton (1982). Similarly, for non linear temperature profiles onset of convection is predicted by using two-dimensional analysis [Moore and Weiss 1973].

2.1 Numerical model

2.1.1 Mathematical formulation

The system of interest in present study is assumed to be in unsteady state and the fluid motions to be laminar. Variation in density has been considered only in the body force term of the momentum equation and termed as Boussinesq approximation. Thermo-physical properties have been taken constant in the transport equations. The resulting dimensional form of conservation equations of mass, momentum, energy and species are, respectively,

Continuity:

$$\frac{\partial U}{\partial X}+\frac{\partial U}{\partial Z}=0 \tag{2.1}$$

X- Momentum:

$$\frac{\partial U}{\partial t}+U\frac{\partial U}{\partial X}+W\frac{\partial U}{\partial Z}=-\frac{1}{\rho_o}\frac{\partial p_d}{\partial X}+\nu\left(\frac{\partial^2 U}{\partial X^2}+\frac{\partial^2 W}{\partial Z^2}\right) \tag{2.2}$$

Z-Momentum:

$$\frac{\partial W}{\partial t}+U\frac{\partial W}{\partial X}+W\frac{\partial W}{\partial Z}=-\frac{1}{\rho_o}\frac{\partial p_d}{\partial Z}+\nu\left(\frac{\partial^2 W}{\partial X^2}+\frac{\partial^2 W}{\partial Z^2}\right)+\underline{g(\beta_T\Delta T-\beta_S\Delta S)} \tag{2.3}$$

Concentration equation:

$$\frac{\partial S}{\partial t}+U\frac{\partial S}{\partial X}+W\frac{\partial S}{\partial Z}=k_s\left(\frac{\partial^2 S}{\partial X^2}+\frac{\partial^2 S}{\partial Z^2}\right) \tag{2.4}$$

Energy equation:

$$\frac{\partial T}{\partial t}+U\frac{\partial T}{\partial X}+W\frac{\partial T}{\partial Z}=k_T\left(\frac{\partial^2 T}{\partial X^2}+\frac{\partial^2 T}{\partial Z^2}\right) \tag{2.5}$$

Here U is the horizontal velocity of fluid (in X direction), W the fluid velocity in Z direction, p_d the dynamic pressure, ρ_o the reference density, β_S salinity expansion coefficient, β_T thermal expansion coefficient, ν the kinematic viscosity, k_T thermal diffusivity, k_S the mass

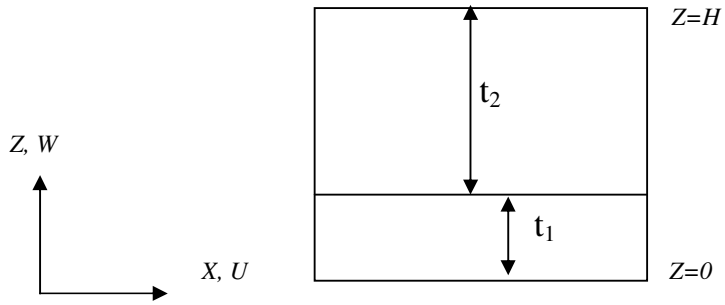

Figure 2.1 Schematic diagram of domain

diffusivity, S the salinity and T the temperature. Here, $\Delta S = S - S_0$ and $\Delta T = T - T_0$.

The geometry and co-ordinate system are illustrated in figure 2.1. The depth of the total layer height H (=thickness of bottom layer t_1+thickness of top layer t_2) is chosen as the characteristic length. We have defined t_1/t_2 as thickness ratio.

The underlined term in equation 2.3 is the buoyancy term. It appears because density is taken as the function of concentration and temperature. By using Taylor series expansion for small changes in temperature and salinity and neglecting the second and higher order terms, the density variation at constant pressure may be expressed as in the following equation of state:

$$\rho = \rho_o \left[1 - \beta_T (T - T_0) + \beta_S (S - S_o)\right] \tag{2.6}$$

Where ρ_o denotes the density of the fluid at a reference temperature. Here S_0 and T_0 are the reference salinity and temperature. β_S and β_T are the coefficient of saline expansion at constant pressure & temperature and the coefficient of thermal expansion at constant pressure and salinity and defined as:

$$\beta_s = \frac{1}{\rho_0}\left[\frac{\partial \rho}{\partial S}\right]_{p,T} ; \beta_T = -\frac{1}{\rho_0}\left[\frac{\partial \rho}{\partial T}\right]_{p,S}$$

Note that the sign of saline expansion coefficient is positive. In physical terms it means that an increase in the concentration induces an increase in density of the fluid and vice versa.

2.1.2 Dimensionless equations

The problem of mass transfer so far described is governed by several parameters like fluid properties [density, mass diffusivity, momentum diffusivity, and volumetric expansion coefficient], the geometrical dimensions like enclosure height, and property like concentration of the system. The number of independent parameters can be reduced by normalizing the governing equations. The conservation equations for two-dimensional salt diapirs were non-dimensionalised using the following scaling: the depth of the total layer

height H is chosen as the characteristic length, velocity (U, W), salinity (S), pressure (p_d) and time (t) are non-dimensionalised as

$$x = \frac{X}{H}; z = \frac{Z}{H}; u = \frac{U}{(k_t / H)}; w = \frac{W}{(k_t / H)};$$

$$S^* = \frac{S - S_0}{S_T - S_0}; T^* = \frac{T - T_0}{T_T - T_0}; t^* = \frac{t}{H^2 / k_T}; P = \frac{P_d}{\rho_0 k_T^2 / H^2} \tag{2.7}$$

Where S_0 and T_0 are the concentration and temperature of the bottom layer and S_T and T_T are concentration and temperature of the top layer respectively. On introducing the above non-dimensional variables, the governing equations (2.1) through (2.5) reduce to the following form (star* symbol dropped for convenience):

Continuity equation:

$$\frac{\partial u}{\partial x} + \frac{\partial w}{\partial z} = 0 \tag{2.8}$$

X-Momentum equation:

$$\frac{\partial u}{\partial t} + u\frac{\partial u}{\partial x} + w\frac{\partial u}{\partial z} = -\frac{\partial p}{\partial x} + \Pr\left(\frac{\partial^2 u}{\partial x^2} + \frac{\partial^2 u}{\partial z^2}\right) \tag{2.9}$$

Z-Momentum equation:

$$\frac{\partial w}{\partial t} + u\frac{\partial w}{\partial x} + w\frac{\partial w}{\partial z} = -\frac{\partial p}{\partial z} + \Pr\left(\frac{\partial^2 w}{\partial x^2} + \frac{\partial^2 w}{\partial z^2}\right) - Ra_s \Pr.S + Ra_T \Pr.T \tag{2.10}$$

Concentration equation:

$$\frac{\partial S}{\partial t} + u\frac{\partial S}{\partial x} + w\frac{\partial S}{\partial z} = \frac{\Pr}{Sc}\left(\frac{\partial^2 S}{\partial x^2} + \frac{\partial^2 S}{\partial z^2}\right) \tag{2.11}$$

Energy equation:

$$\frac{\partial T}{\partial t} + u\frac{\partial T}{\partial x} + w\frac{\partial T}{\partial z} = \left(\frac{\partial^2 T}{\partial x^2} + \frac{\partial T^2}{\partial z^2}\right) \tag{2.12}$$

2.1.3 Non-dimensional parameters

The important dimensionless governing parameters emerges from the above equations are salinity Rayleigh number (Ra_S),thermal Rayleigh number (Ra_T), Prandtl number (Pr) and Schmidt number(Sc) and are defined as

$$Ra_S = \frac{g\beta_S \Delta S H^3}{\nu . k_T}; Ra_T = \frac{g\beta_T \Delta T H^3}{\nu . k_T}; Sc = \frac{\nu}{k_s}; \Pr = \frac{\nu}{k_T}$$

2.1.4 Initial and boundary conditions

In a one component system light fluid layer at the bottom and heavy sugar solution is at the top. The step profiles are chosen to simulate the two-layer laboratory experiments. Most of the previous laboratory experiments, in which fluxes and structures have been studied, are two-layer experiments.

The initial profiles in non-dimensional forms are:

$S = 0$ z = [0 a]

$S = 1$ z = [a 1]

$T = 1$ z = [0 a]

$T = 1$ z = [a 1]

Here a Є (0, 1) and the thickness ratio (TR) is defined as a/(1-a).

The initial profile is made same as in the experimental input as shown in figure 2.2, as the variation of density is predominately due to concentration, in our simulation, T is taken as constant (=1).

2.1.5 Velocity boundary conditions

Slip velocity boundary conditions are applied to side walls.

$$u(0,z) = u(1,z) = 0; \quad \frac{\partial w}{\partial x} = 0 \qquad (2.13)$$

No slip is applied at the top and bottom walls.

$$u(x,\ 0) = 0;\ \ u(x,\ 1) = 0 \tag{2.14}$$

At the top and bottom the walls are rigid. No mass flux was allowed to cross the system.

$$w(x,\ 0) = 0;\ \ w(x,\ 1) = 0 \tag{2.15}$$

2.1.6 Temperature and concentration boundary conditions

Since no mass or heat and mass flux were allowed to cross the system boundaries, adiabatic boundary conditions were applied on all the four walls.

$$\frac{\partial S}{\partial x} = \frac{\partial S}{\partial z} = 0\ ,\ \frac{\partial T}{\partial x} = \frac{\partial T}{\partial z} = 0 \tag{2.16}$$

2.2 Numerical methodology

The computational domain was discretized into small control volumes. The set of governing equations was integrated over each control volume. The finite volume method and Semi Implicit Method for Pressure-Linked Equations Revised (SIMPLER) algorithm was used for

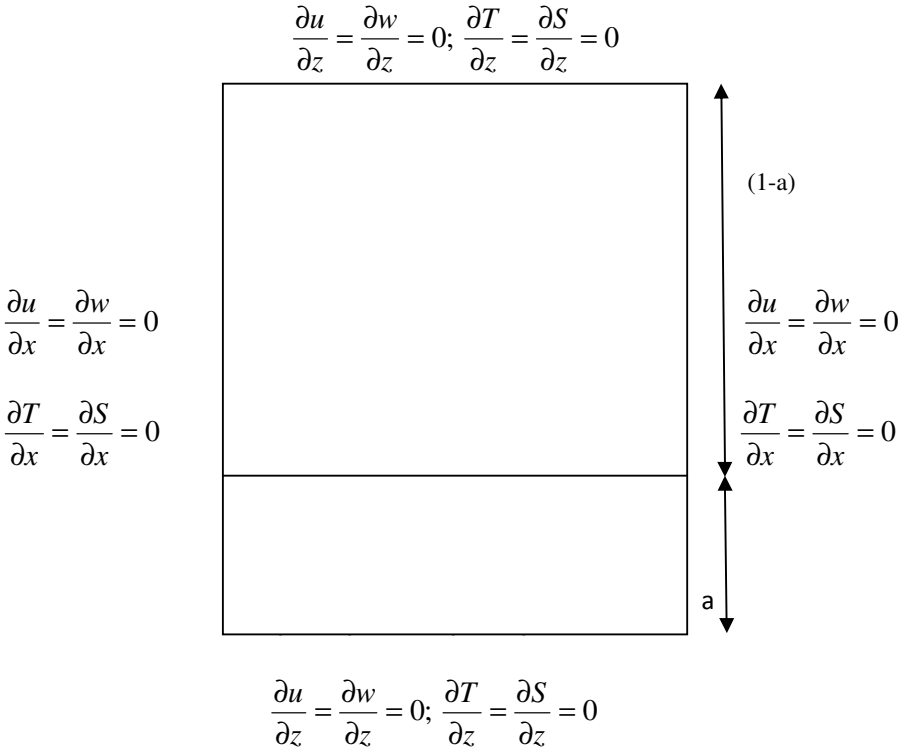

Figure 2.2: A schematic of the computational domain with initial and boundary conditions. Slip condition for velocity on all the walls is applied. No heat and mass transfer was allowed across the system boundaries. A step profile for concentration and temperature is employed as initial condition similar to the laboratory two-layer setup.

the discretization and solutions of these equations with the relevant boundary conditions. Details of this algorithm are given in Patankar (1980). The equations were split with the use of Alternate Direction Implicit (ADI) method to get *tridiagonal systems* and the solutions are obtained by marching in time. A brief outline of ADI method and SIMPLER algorithm will be given in following sections.

2.2.1 ADI method

Alternate Direction Implicit method is an efficient technique for splitting the equation to get *tridiagonal systems*. In case of a two dimensional heat conduction equation, for example, the forward difference in time and central in space (FTCS) results in a conditionally stable solution. In order to get rid of this restriction in solving the problem, an implicit scheme can be used. However, an implicit scheme results in a *pentagonal system* of matrix to solve the constants. Solving a *pentagonal system* is cumbersome and very time consuming process. So, in order to avoid this hassle, the ADI scheme was used. Considering the two dimensional diffusion equation:

$$\frac{\partial T}{\partial t} = k_T\left(\frac{\partial^2 T}{\partial X^2} + \frac{\partial^2 T}{\partial Z^2}\right) \tag{2.17}$$

Using FTCS formulation of the above equation we get,

$$T_{i,j}^{n+1} - T_{i,j}^{n} = k_t \Delta t\left(\frac{T_{i+1,j}^{n} - 2T_{i,j}^{n} + T_{i-1,j}^{n}}{\Delta X^2} + \frac{T_{i,j+1}^{n} - 2T_{i,j}^{n} + T_{i,j-1}^{n}}{\Delta Y^2}\right) \tag{2.18}$$

Here *n* is the *nth* time step. The results produced using above equation are of the accuracy of Δt, $\Delta X^2$and ΔY^2. However this solution is only conditionally stable for

$$\frac{k\Delta t}{\Delta X^2} + \frac{k\Delta t}{\Delta Y^2} = \leq 0.5 \tag{2.19}$$

When equal grid spacing is used in both the directions then the stability restriction will get doubled and this may require very low time steps to get converge solutions. The price is high computation time. To avoid this restriction, implicit scheme for the same problem is considered as follows:

$$T_{i,j}^{n+1} - T_{i,j}^{n} = k_T \Delta t \left(\frac{T_{i+1,j}^{n+1} - 2T_{i,j}^{n+1} + T_{i-1,j}^{n+1}}{\Delta X^2} + \frac{T_{i,j+1}^{n+1} - 2T_{i,j}^{n+1} + T_{i,j-1}^{n+1}}{\Delta Y^2} \right) \tag{2.20}$$

However, this equation results in a pentagonal system of equations. Alternatively, the equation can be split into two equations with the use of Alternating Direct Implicit scheme to solve them by making the two tridiagonal system of equations in two directions or alternating the direction.

$$T_{i,j}^{n+1/2} - T_{i,j}^{n} = 2k_t \Delta t \left(\frac{T_{i+1,j}^{n+1/2} - 2T_{i,j}^{n+1/2} + T_{i-1,j}^{n+1/2}}{\Delta X^2} + \frac{T_{i,j+1}^{n} - 2T_{i,j}^{n} + T_{i,j-1}^{n}}{\Delta Y^2} \right) \tag{2.21}$$

$$T_{i,j}^{n+1} - T_{i,j}^{n+1/2} = 2k_t \Delta t \left(\frac{T_{i+1,j}^{n+1/2} - 2T_{i,j}^{n+1/2} + T_{i-1,j}^{n+1/2}}{\Delta X^2} + \frac{T_{i,j+1}^{n+1} - 2T_{i,j}^{n+1} + T_{i,j-1}^{n+1}}{\Delta Y^2} \right) \tag{2.22}$$

Note that in this system of two equations, equation (2.21) is implicit in *X* direction and explicit in *Y* direction and known as *X* sweep. Thomas algorithm is used to invert the tridiagonal matrix obtained from (2.21). The data provided by equation (2.22) to get the value of temperature, which is implicit in *Y* direction and explicit in *X* direction. We need to iterate these equations for getting solution at each time step. This method is unconditionally stable for this is an implicit scheme. It is accurate in second order in time and space.

2.2.2 SIMPLER algorithm

The general dimensional form of a transient conservation equation for a general variable, φ, with advection, diffusion and source terms in Cartesian coordinate is given by

$$\frac{\partial(\rho\varphi)}{\partial t}+\frac{\partial(\rho U\varphi)}{\partial X}+\frac{\partial(\rho W\varphi)}{\partial Z}=\frac{\partial}{\partial X}\left(\varepsilon\frac{\partial\varphi}{\partial X}\right)+\frac{\partial}{\partial Z}\left(\varepsilon\frac{\partial\varphi}{\partial Z}\right)+\Sigma \qquad (2.23)$$

Here, *U* and *W* are the horizontal and vertical velocities, ε is the diffusion coefficient of φ and Σ is the volumetric source term. Σ is zero in our case. The non-dimensional form of above equation has been numerically integrated in this thesis. When (2.23) is integrated over space, in *X* and *Z* directions and over time *t*, a set of algebraic finite difference equations is obtained for each grid location. ADI method, discussed in section §2.2.1, is used to get the system of tridiagonal matrix. Thomas algorithm is used for inverting the matrix to get the solution.

The variable φ in (2.23) can be any one of the velocity components *U, W* (2.9 or 2.10), temperature or *S* (3.12) but not pressure. The pressure does not obey any type of conservation

law. Therefore, pressure cannot be solved for explicitly. However, the pressure field used must produce a velocity field that satisfies mass conservation equation. The SIMPLER algorithm includes of the following steps:

1. Initial conditions of the system invoked.

2. *X* and *Z* momentum equations are solved for *U* and *W*

3. The pressure field is determined from the Poisson equation for pressure using the velocity field from the previous step.

4. The pressure distribution is used to determine a new velocity field.

5. A pressure correction for this velocity field is determined to satisfy the mass conservation.

6. The velocity field is corrected using the corrected pressure. This new velocity field satisfies the mass conservation.

7. Energy equation (2.11) and concentration equation (2.12) are solved.

8. Convergence is checked at this stage. If the required convergence criteria is attained, the values of all the variables are updated and marched to next time step, otherwise the operations from step 2 to 8 is repeated at the same time level, till the set criteria of convergence is achieved.

The codes were run on Chandrayaan cluster at JNCASR computing facility. Code validation is done by considering single-diffusive and double diffusive convection problems. The accuracy of the numerical code is examined by reproducing the published results. The results of the benchmark solution given by de Vahl Davis & Jones (1983) for single diffusive component, natural convection in a square cavity were reproduced. Sreenivas et. al. 2009, have used this code to study the relationship between finger-width, velocity and fluxes of double diffusive fingers, and details of code validation are available in this paper.

2.3 Results from simulations

We will present here the effect of viscosity, density contrast and layer thickness ratio on diapiric structures. For this study we have taken constant grid sizes. We will also describe the behavior of diapiric structures as function of Ra_S.

Our code is written for double diffusive convection (i.e. we can study the effect of temperature and salinity gradient) in the form of dimensionless number *Gr* and *Sc*. For our study we have considered negligible effect of temperature. So ΔT has been taken as zero and only effect of concentration is studied. We have carried out simulations in a two layer system in which heavy fluid [*S=1, T=1*] overlies lighter fluid [*S=0, T=1*]. Compositional Grashof number (Gr) is defined as the ratio of buoyancy to viscous forces:

$$Gr = \frac{g\beta_S \Delta S.H^3}{\nu^2}$$

2.3.1 Layer thickness effect on diapiric structures

To study the effect of layer thickness ratios, we have done simulations with constant Gr number (Gr=40000) and Sc number (Sc=1000) and have varied thickness ratio from 1/19 to 11/9. In further study we have increased Gr number (Gr = 90000) and kept Sc number same. We again varied layer thickness ratio from 1/19 to 11/9 and have study the changes in diapiric structure formation.

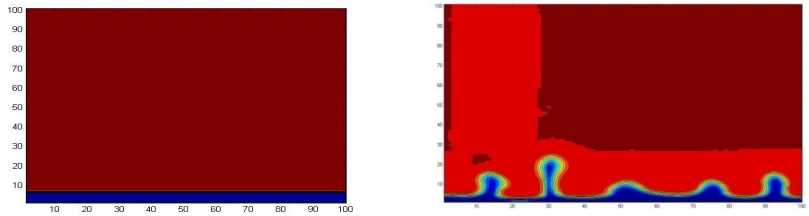

t=0 (a) t1=8.9X10^{-5}

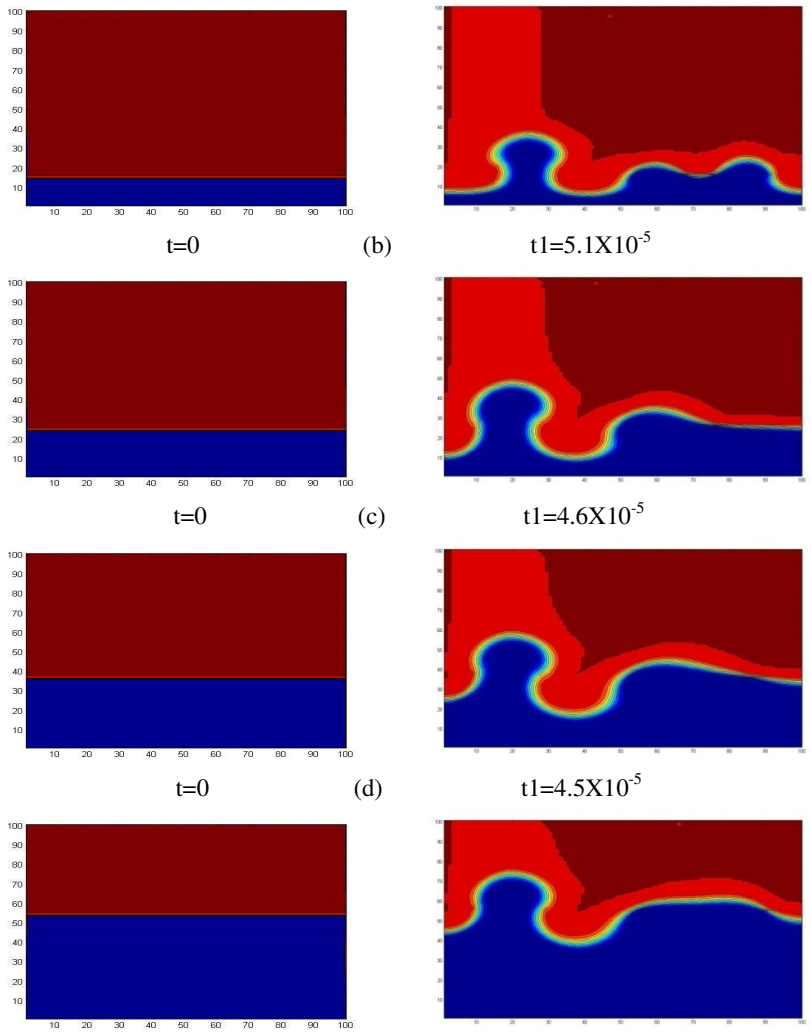

Figure 2.3: contour plot of concentration
Effect of layer thickness ratios (TR) for constant Gr (40000) and Sc (1000). (a) TR =1/19 (b) TR = 3/17 (c) TR = 5/15 (d) TR = 7/13 (e) TR = 11/9. [Right side of figure 2.2a to 2.2e are at t=0 and left side are after time t1, where t1 is the dimensionless time taken to grow diapirs upto same height]

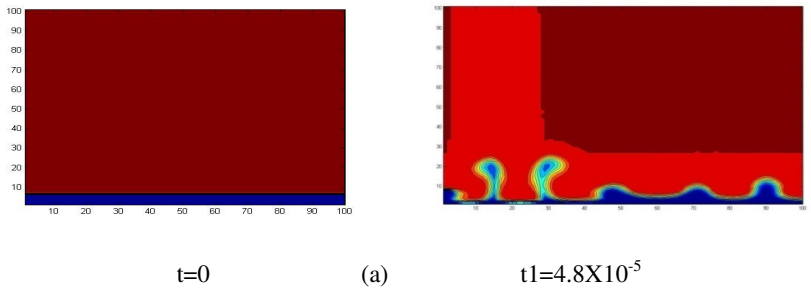

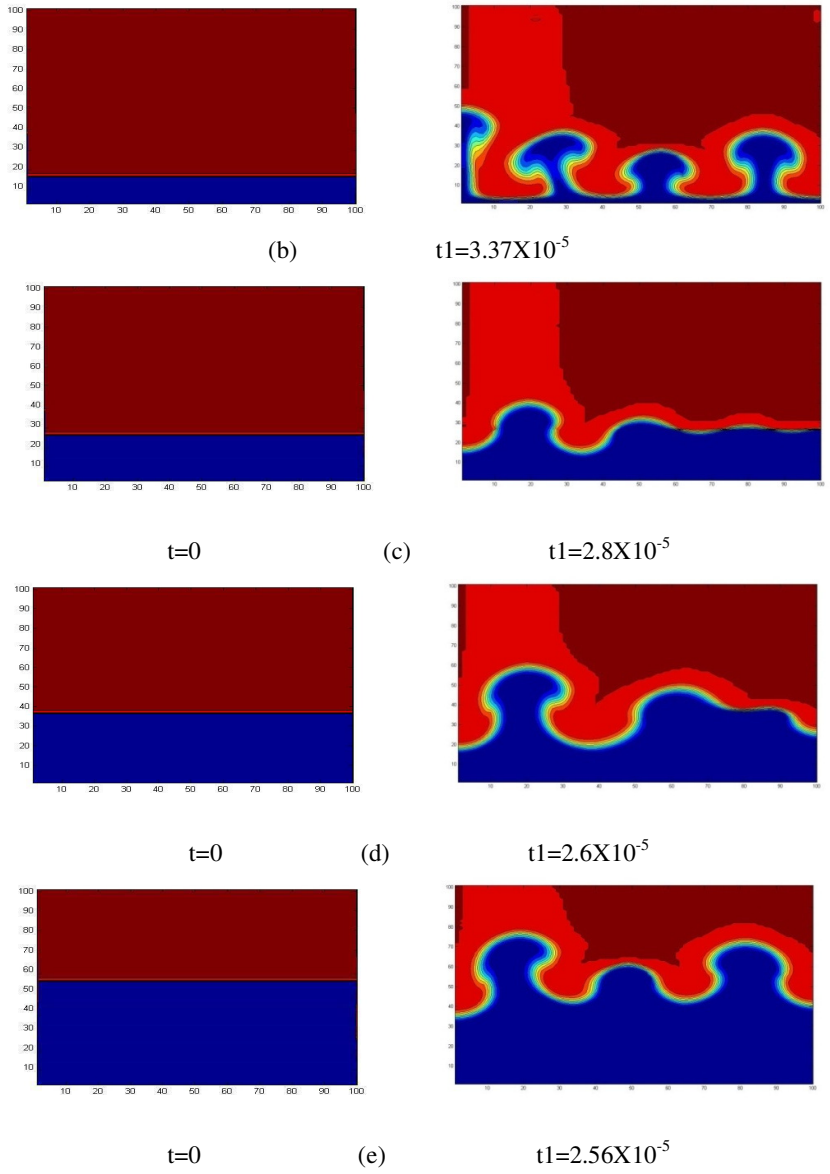

Figure 2.4: contour plot of concentration
Effect of layer thickness ratios (TR) for constant Gr (90000) and Sc (1000). (a) TR =1/19 (b) TR = 3/17 (c) TR = 5/15 (d) TR = 7/13 (e) TR = 11/9. [Right side of figure 2.2a to 2.2e are at t=0 and left side are after time t1, where t1 is the dimensionless time taken to grow diapirs upto same height]

In figure 2.2a to 2.2e results from simulations are shown for constant Sc (1000) and Gr (40000) with varying thickness ratios (TR). We can see here the decrease in the number of diapiric structures and increase in their thickness as we increase the thickness ratio TR.

In figure 2.3a to 2.3e results from simulations are shown for constant Sc (1000) and Gr (90000) with variation in thickness ratios (TR). We can see here the decrease in the number of diapiric structures and increase in their thickness as we increase the thickness ratio TR. We can also see qualitative changes in comparison to previous simulations (see figure 2.2). Changes in the number of structures, their thickness as well as spacing between them vary when we vary our Gr number 40000 to 90000.

2.3.2 Gr number effect on diapiric structures

To study the effect of Gr number on diapiric structures, we have done simulations with constant Sc number and layer thickness ratios and have varied Gr number. To study the effects of small changes in Gr number, we have done simulations for Gr number variation from 40000 to 90000. Further to study over a large change in Gr number, we have varied Gr number from 10^4 to 10^9.

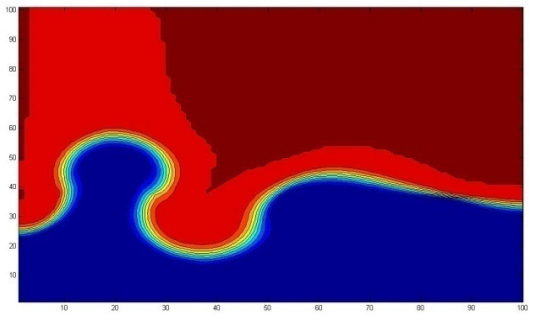

(a) t1=4.68X10^{-5}

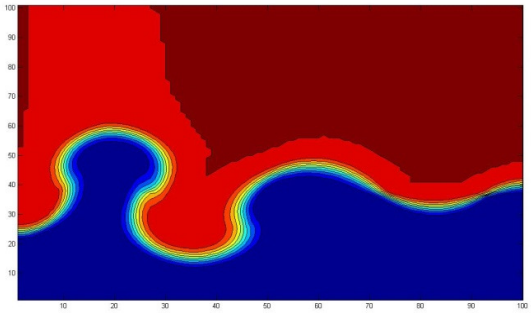

(b) t2=4.68X10^{-5}

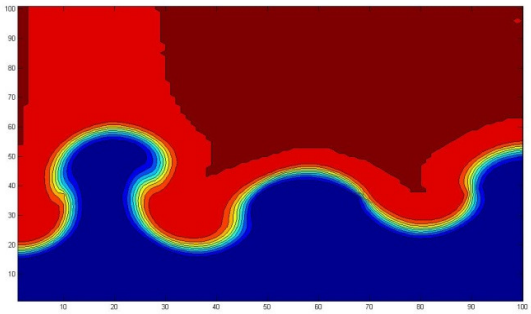

(c) t3=3.87X10^{-5}

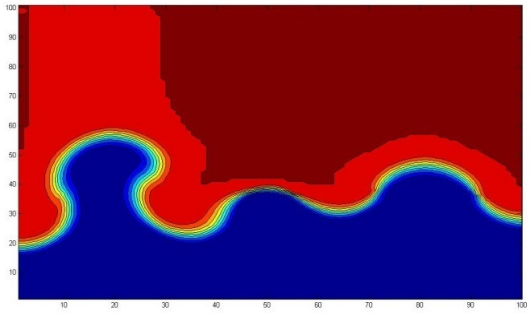

(d) t4=3.3X10^{-5}

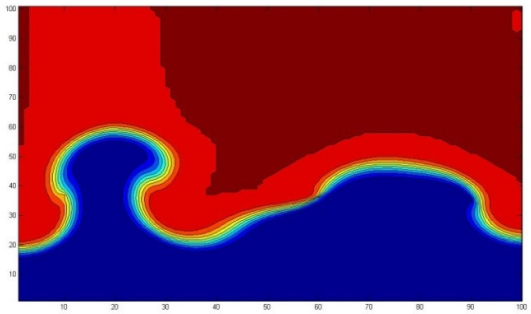

(e) t =3.12X10^{-5}

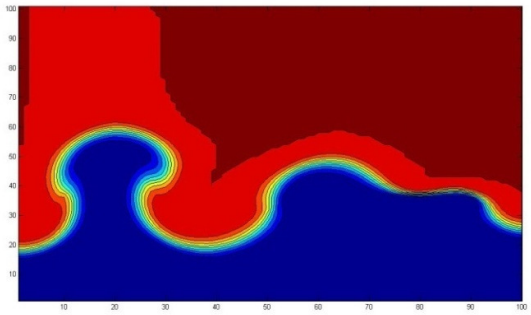

(f) t=2.87X10^{-5}

Figure 2.5: contour plot of concentration
Effect of small variation of Gr number for constant Sc (1000) and layer thickness ratio (TR =7/13). (a) Gr = 40000 (b) Gr = 50000 (c) Gr = 60000 (d) Gr = 70000 (e) Gr = 80000 (f) Gr = 90000. [Where t1 is the dimensionless time taken to grow diapirs upto same height]

In figure 2.4a to 2.4f results from simulations are shown for constant Sc (1000) and TR (7/13) with small variation in Gr. If we see carefully, minor increment in the number of diapiric structures and decrease in their thickness could be observed as we increase the Gr number.

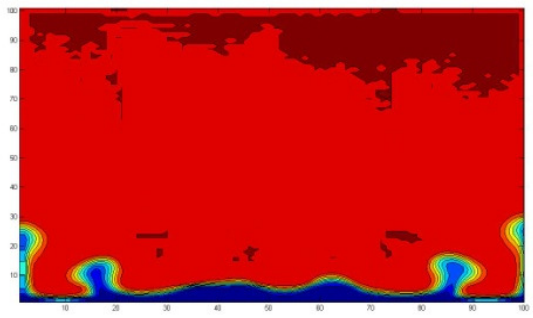

(a) t=4.6X10^{-5}

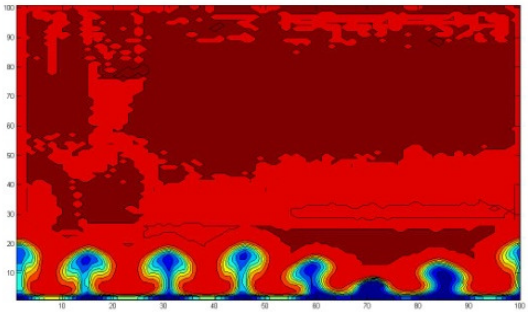

(b) t= $7.5X10^{-6}$

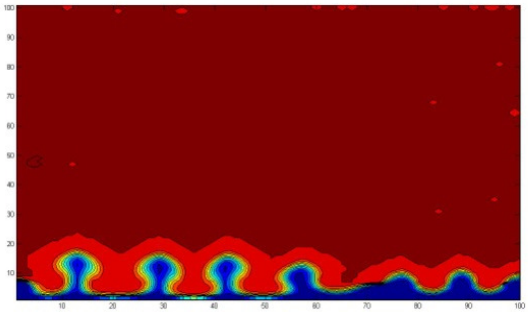

(c) t=$1.5X10^{-6}$

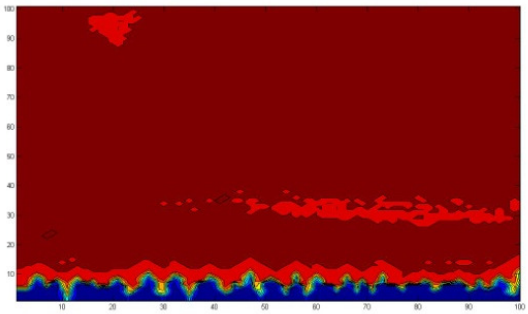

(d) t=$3.75X10^{-7}$

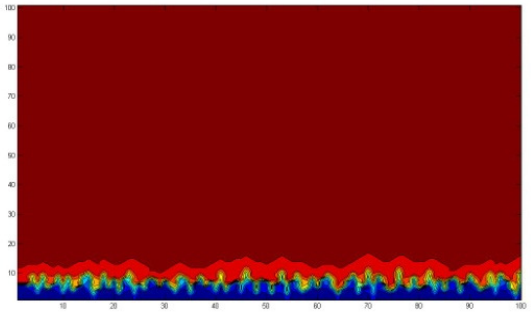

(e) t=5.0X10^{-8}

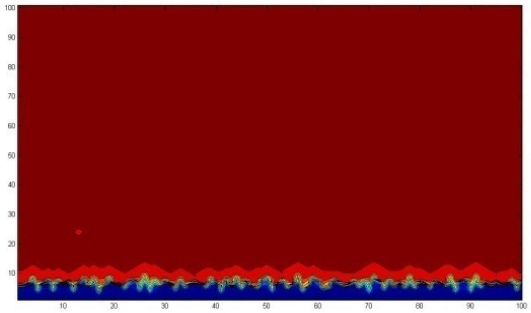

(f) t=3.0X10^{-8}

Figure 2.6: contour plot of concentration
Effect of large variation in Gr number for constant Sc (1000) and layer thickness ratio (TR = 1/19). (a) Gr = 10^5 (b) Gr = 10^6 (c) Gr = 10^7 (d) Gr = 10^8 (e) Gr = 10^9 (f) Gr = 10^{10} [t is dimensionless time required for evolving similar height of diapirs].

For small changes in Gr number, changes in diapiric structures were too small to observe. But for sharp changes in Gr number, number of structures increases dramatically as well as thickness and spacing decreases.

2.3.3 Sc number effect on diapiric structures

To study the effect of Sc number on the dynamics of diapiric structures the simulations have been done for constant Gr number and layer thickness ratio (Gr = 10^4 and 10^9, TR = 1/19). The simulations have been done for different Sc numbers (Sc = 10^3, 10^4, 10^7 and $10^{9)}$. In the results we did not see any changes in the parameters like number of structures, spacing

between and thickness but the time required for evolution of same length of diapirs increases dramatically. By definition Sc number is combination of kinematic viscosity and diffusivity. For constant diffusivity variation in Sc number is increase in viscosity only. The viscosity of solution controls the rate of convection of phenomena. That may be the reason for this large change in the time required for evolution of same length.

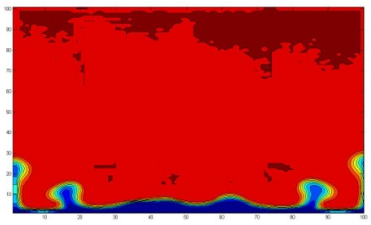

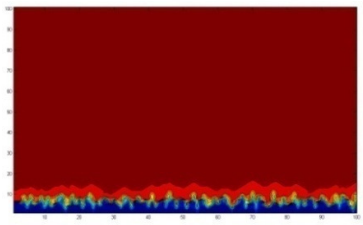

(a) t=6.25X10^{-5} Sc =10 (A) t=3.0X10^{-7}

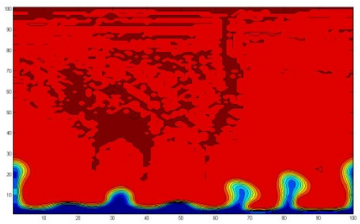

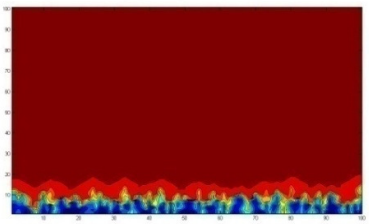

(b) t=8.2X10^{-5} Sc=10^{4} (B) t=7.1X10^{-7}

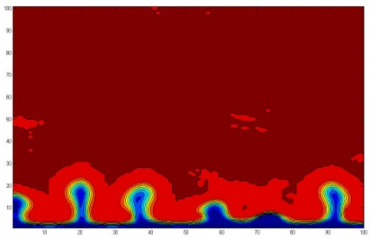

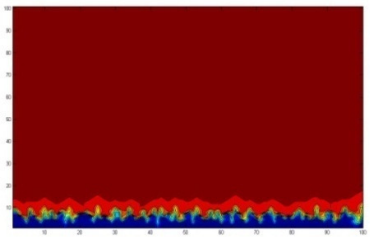

(c) t=9.8X10-5 Sc=10^{7} (C) t=8.3X10^{-7}

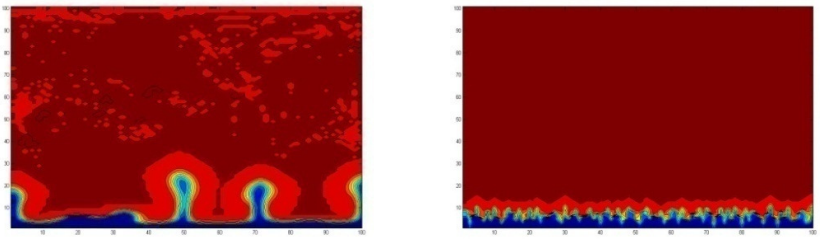

(d) $t=1.1X10^{-4}$ $Sc=10^{9}$ (D) $t=9.7X10^{-7}$

Figure 2.7: contour plot of concentration
Effect of variation in Sc number for constant Gr 10^4 (a,b,c,d) & 10^9 (A,B,C,D) and layer thickness ratio (TR = 1/19)

In the chapter 4, we will analyze these results in details. A series of 24 numerical simulations was performed in a two-layer system, covering a wide range of density, layer thickness ratio and Rayleigh numbers. Results presented in the next chapter on salt diapirs are carried out from the present code. We will investigate these simulation results from experiments and will conclude the work.

Chapter 3

Experimental Setup and Measurements

In this chapter the effect of viscosity and layer thickness ratios on diapiric structures, their time evolution and the effect of Rayleigh number on diapiric structures will be discussed with the help of laboratory experiments. Very few experiments are available in the scientific literature that reports the effect of Rayleigh numbers on salt diapir structures. The experiments have been conducted in a square cross-section tank. The convection is driven by concentration across the interface between two fluid layers of equal viscosity. CMC (Carboxy Methyl Cellulose) has been used to vary the viscosity of the water and sugar to increase the density. The viscosity of solution is enhanced and the effect of viscosity on the diapiric structures has been studied. In this chapter, the experimental setup and methodology is described in detail.

3.1 Experimental setup

Figure 3.1 shows a schematic of construction details of the experimental setup. A glass tank of inner dimension 30cmX30cmX20cm and wall thickness of 10mm has been fabricated. Tank is open at the top. It hangs on a cylindrical rod connected to a portable metallic stand. The tank can be rotated using a handle connected to this rod in order to invert the tank. A sealing lid has been provided to seal the tank from top after filling it up with two fluid layers. This sealing prevents any leakage during the experiments after inverting the setup by 180^0 to make the unstable density configuration.

In a two layer system placing the layers one above the other with minimum disturbance was crucial to the evolution of diapirs. Extreme care was taken to minimize the turbulence mixing

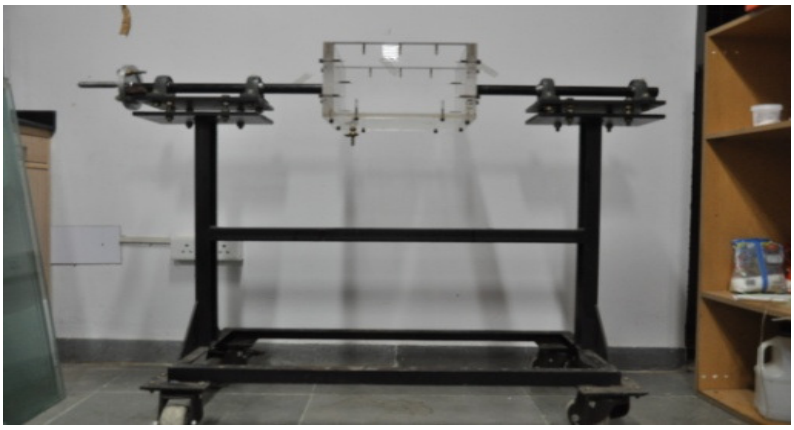

Figure 3.1: Schematic diagram showing the experimental setup

at the interface, while pouring the lighter fluid layer over the dense fluid layer. Mixing at the interface between two layers depends upon many factors. Some of the important factors that have to be keenly noted are the rate of pouring, density difference and viscosity of fluid layers. When the fluid used for experiments was less viscous, reducing the mixing rate at the interface was a tedious task. When fluid of enhanced viscosity was used, mixing at the interface was not a big problem. Experiments reveal that high viscosity reduces the turbulent mixing at the interface.

3.2 Bubble removing mechanism and setup

The solutions used in the initial experiments were full of bubbles. At the time of mixing CMC into water and sugar solutions, these bubbles were formed. It was a necessity to remove these bubbles from the solutions. During the experiments these bubbles create light spots as the laser sheet passes through the solution. These bubbles also change the properties of solutions like density and viscosity. Removal of bubbles was a very challenging and time consuming process.

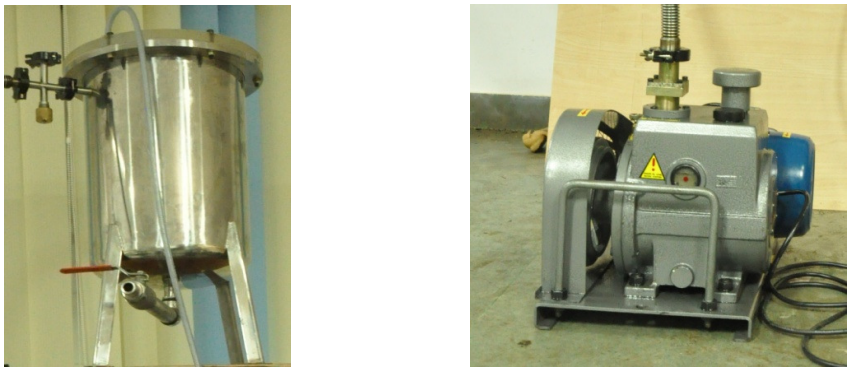

(a) **(b)**

Figure 3.2 (a) Vacuum Chamber (b) Vacuum pump

In order to remove these bubbles from the solution a cylindrical vacuum chamber with a capacity of 22 liters was used [figure 3.2a]. This cylinder consists of an opening at the top, an outlet at the bottom and an opening with valve to connect a vacuum pump [figure 3.2b]. A transparent lid has been provided to prevent any leakage from the top at the time of degassing. High viscous dense solution was poured inside this chamber and sealed from the top.

The vacuum is created by connecting the vacuum pump to this chamber and running the pump for 3-6 hours depending on the viscosity of solutions. Solution is left inside the chamber for a few hours at this low pressure so that bubbles can rise to the surface. After few hours the vacuum is removed and this solution is left for a few hours to kill the bubbles in order to get a clear and transparent solution. The time taken for the bubble removal process is 1-2 days per batch of solution.

This clear solution is transferred from vacuum chamber to the experimental tank as bottom layer using the outlet of the chamber. Now the same process is repeated for the lighter solution and is transferred to the tank.

3.3 Setup to accelerate the out flow from vacuum chamber

A setup was designed for the outflow of viscous solution from the vacuum chamber. As the solution used in the experiments is highly viscous and the outlet valve of vacuum chamber is of very small cross-section, it was very hard to drive out from the valve. To overcome this problem the vacuum chamber with solution inside is placed at a height of one meter to generate pressure head to increase the flow velocity of solution at the outlet valve. This step was not sufficient as the viscosity of solution was very high. To increase the velocity further at the outlet and reduce the time to get the solution out from chamber a cycle paddle pump was added to the vacuum chamber. Putting the vacuum chamber at the height of one meter and pumping the air from the top of the vacuum chamber helped in getting required outflow.

3.4 Traverse mechanism

In the experiments conducted earlier, images of a particular vertical plane were captured. In this way the information of other region in the domain was missing. Instead of studying this phenomenon in a particular plane of the domain, as we were interested in studying the phenomena in full region inside the tank or 3D structure formations in the full domain. For this purpose a temporary and simple setup was designed. An aluminum rod of square cross-section was attached to the wall. The optics and continuous green laser is mounted on a small wooden box that can slide on this rod as shown in figure 3.3. A Centimeter scale was marked on this rod using a permanent marker so that an accurate horizontal positioning of the laser sheet is possible. Sliding the wooden box on this rod, eleven vertical planes with 2.5cm spacing were captured. The captured images were processed and analyzed using Matlab software.

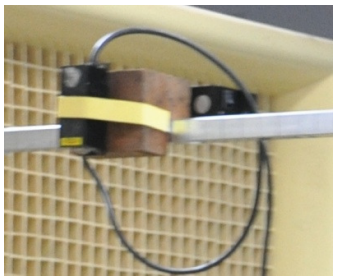

Figure 3.3: Traverse and laser arrangement

3.5 Laser and optics

In the experiments, 532 nm solid-state semiconductor diode continuous laser of 50 mW power (manufactured by Shangai Dream Lasers, China) has been used for flow visualization.

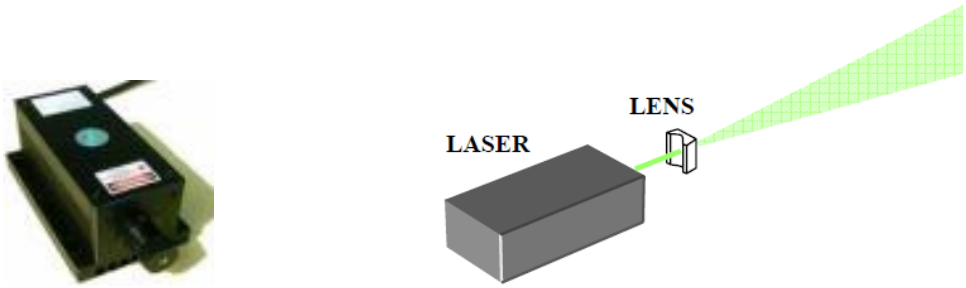

(a) **(b)**

Figure 3.4: (a) Laser (b) Schematic of laser and optic arrangement

The light from the laser has been passed through the plano-concave lens. In figure 3.4 (b) a schematic of laser and optics arrangements has been depicted. The plano-concave lens is rotated suitably depending on whether horizontal or vertical sheet of light is required.

3.6 Viscosity enhancement

In this section the viscosity enhancement techniques used in the experiments has been discussed. Sodium-Carboxy-Methyl Cellulose (Na-CMC) has been used for the enhancement

of the viscosity of the water. Cellulose ethers are high molecular weight long chain compounds produced by replacing the hydrogen atoms of hydroxyl groups in the anhydrous glucose units of cellulose with alkyl or substituted alkyl groups (reaction of alkali cellulose with sodium mono-chloroacetate under controlled conditions). Na-CMC finds applications in food, pharmaceutical and cosmetic industries where it is used for several functions - as a thickener, suspension aid, binder, stabilizer and film-former. It is used in milk products, dressings, jellies, syrups, in paper industry, water retention aids, oil field chemicals, printing inks, surface coatings, pharmaceuticals, etc. Molecular formula of Na-CMC is R-0-CHCOONa. The molecular weight varies from 21,000- 5,00,000. CMC is basically an anionic water-soluble polymer derived from cellulose. The commercial 'Aqualon' brand '7H4F' grade CMC available from Hercules, Inc, USA (refer Booklet 250, Aqualon, 1999 for technical details) has been used. Viscosity enhancement is the most important property of CMC solutions. The viscosity of CMC solutions increases rapidly with concentration. Generally, CMC solutions are non-newtonian because they change in viscosity with change in shear rate. CMC solutions generally exhibit a pseudo-plastic behavior, i.e. the solutions show a time-independent, shear-thinning behavior under application of shear. Figure 3.5 shows a plot of apparent viscosity v/s shear rate for Newtonian and pseudo-plastic fluids. We will briefly discuss their properties and functions in this section.

When 1 % (by Wt.) of CMC is added to water, the viscosity of the solution increases by a factor of 10,000 to 1,00,000. The amount of increase depends upon the purity of water, the presence of metal ions, solubility and time left for dissolving etc. The property of CMC is that, at very low concentrations of 1% to 5%(by Wt.), the change in other properties, such as

density is not significant (Davaille, 1999).

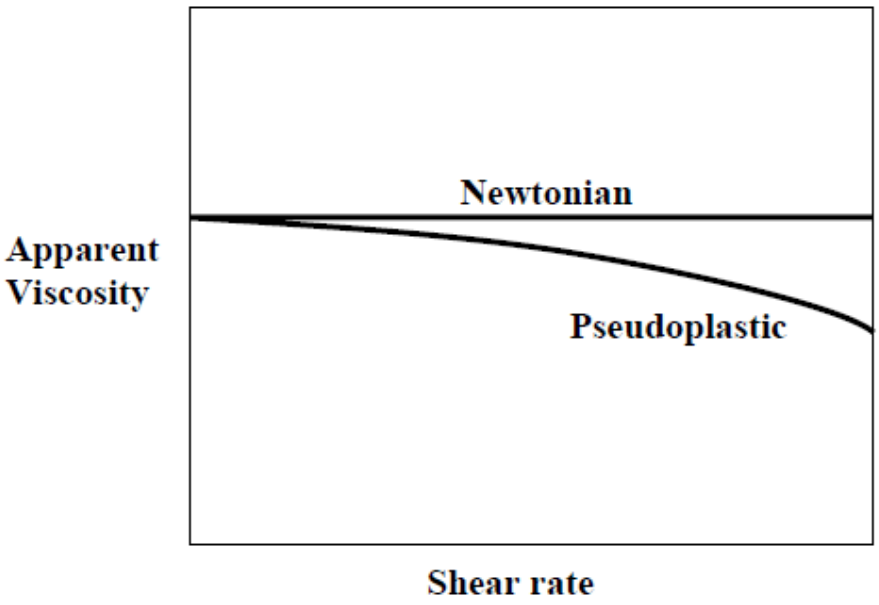

Figure 3.5: Viscosity v/s shear rate for a general fluid

3.7 Solution preparation

CMC solution was prepared by adding CMC powder in water. When CMC was added directly to water, clumps were formed. To overcome this, the fluid was stirred continuously by a motorized stirrer for 24 hr. Then, it was left idle for 48 hr to ensure that CMC is completely dissolved in water.

The main advantage of using CMC is, it allows the viscosity of the fluid to be varied independently, without changing the density. The viscosity of the medium also determines the diffusivity of any component, as mentioned by Laurent, et al (1979) and Davaille (1999), change in the rate of diffusion due to increase in viscosity is postulated to be exponential.

3.8 Viscosity measurements

The viscosity has been measured by two methods – using a rheometer and falling ball method. A computer-controlled rheometer (Rheolyst series AR1000) manufactured by TA Instruments, USA, was used for viscosity measurements. Parallel plate geometry was used with a 400 μm gap between the stationary and rotating plate. It is possible to measure the viscosity at different shear rates varying with time. Viscosities of a number of samples of CMC solutions of different concentrations were measured. Figure 3.6 shows a plot of the absolute viscosity of CMC solutions (in mPas) v/s the concentration of CMC solution (% weight) measured using the rheometer and falling ball method. The falling ball method was used to measure viscosity of CMC solutions in a few cases (shown in figure 3.6). This method uses the Stokes law for a sphere falling through a fluid at low Reynolds numbers.

We have a set of measurements of viscosity of CMC solutions (shown in Fig.10) at discrete values of concentrations from the rheometer [Vivek N.P. et al. 2009, MS thesis]. To find values of viscosity of CMC solutions at intermediate values of concentration (% weight), we fit a 7^{th} order polynomial curve to the data and get an expression for the viscosity as a function of concentration:

$$\mu = 8600.x^7 - 49000.x^6 + 110000.x^5 - 110000.x^4 + 57000.x^3 - 13000.x^2 + 1400.x - 44$$

Where, μ is the absolute viscosity in mPas and c is the concentration of CMC in solution expressed as % weight of CMC in solution. This curve has been extended upto 4 % to find the viscosity of higher values of concentration. Figure 3.7 shows extended plot of viscosity for concentration upto 4%.

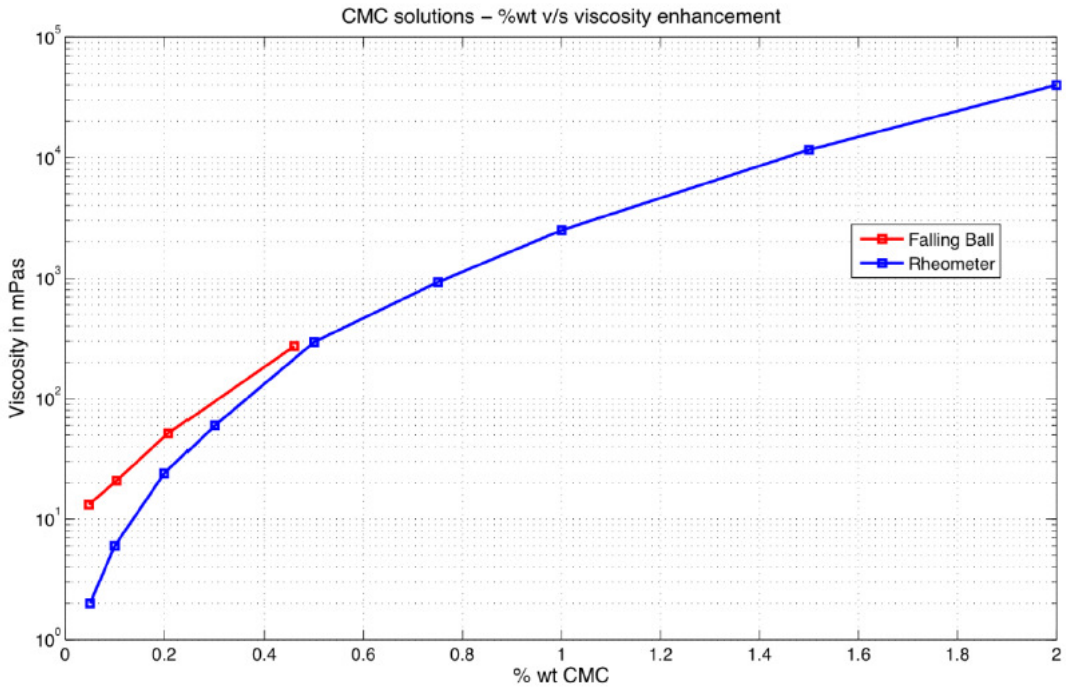

Figure 3.6: Viscosity v/s concentration of CMC [Vivek N.P. et al. 2009]

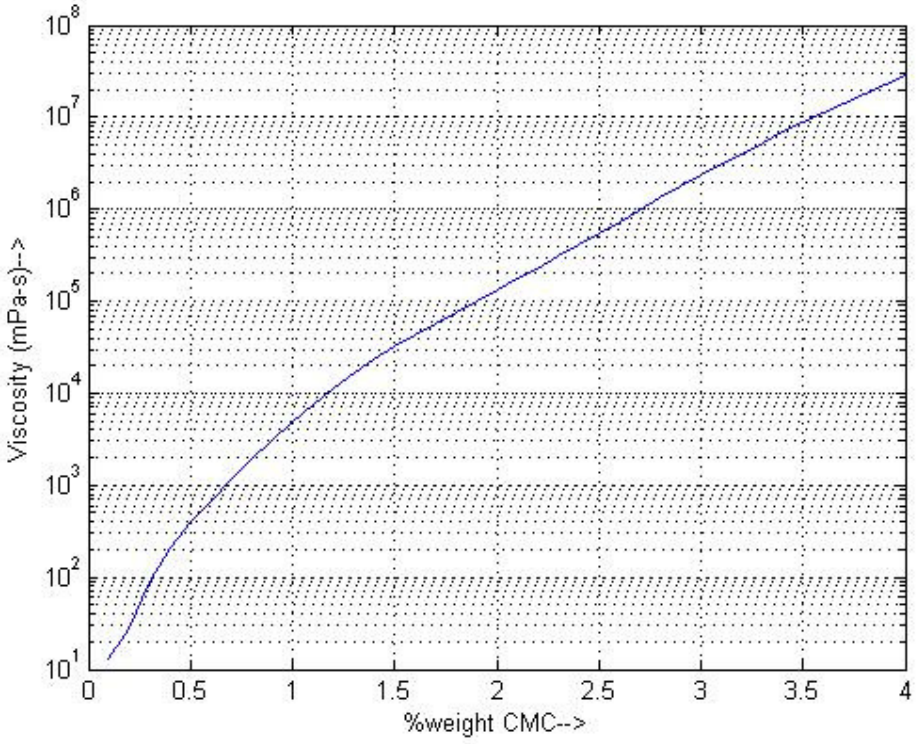

Figure 3.7: Extended plot of viscosity v/s concentration of CMC

3.9 Flow visualization

Flow visualization is a useful technique to qualitatively and quantitatively study the fluid flow phenomena. It often involves the injection of foreign particles into the flow field for making it visible. A non-intrusive Planar-Laser-Induced-Fluorescence (PLIF) technique has been used in which a water-soluble fluorescent dye is used as a scalar flow marker. The structures formed in the test section have been studied by using a laser light source for illumination. The laser beam is converted into a planar sheet using a plano-concave lens. Vertical planar light sheets are used to study the salt structures in vertical sections. Figure 3.8 shows a schematic of the flow visualization process. A small amount (~ 0.2 ppm) of fluorescent Rhodamine-6G dye is dissolved in upper fluid layer. The dye emits a specific wavelength of visible light when excited by an appropriate wavelength of energy. Our laser light is of green color (wavelength of 532 nm) which matches the absorption peak for the Rhodamine dye. Hence, Rhodamine-6G is the preferred dye for our experiments. A small amount of dye added does not affect the flow and the dye act as a passive tracer. Rhodamine dye is highly soluble in water. The phenomenon has been captured using a Nikon D90 Digital SLR camera.

3.10 Experimental procedure

All of our experiments were conducted in the following manner:

1. High viscous sugar solution was prepared by adding sugar and Na-CMC into a known quantity of tap water. Required amount of rhodamine dye (0.2 ppm) was mixed before adding CMC. After removing the bubbles, this solution was transferred to the test section as first layer

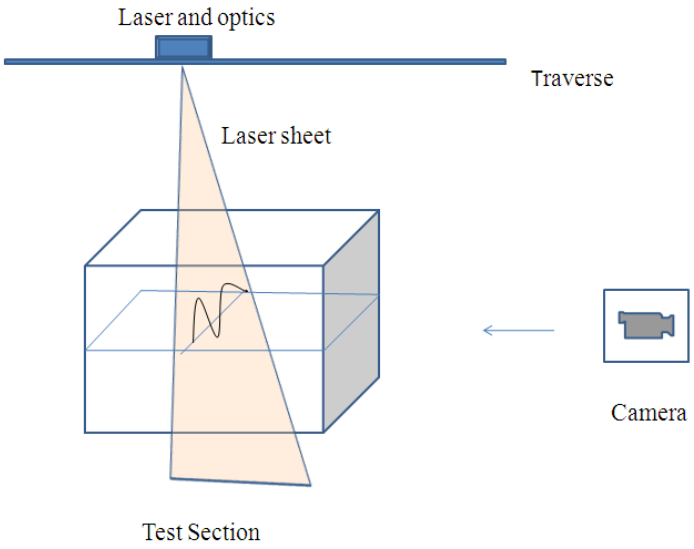

Figure 3.8: A schematic of flow visualization process

1. Before transferring the solution, walls of the test section were cleaned properly from both sides.
2. Lighter solution of same viscosity was prepared by adding Na-CMC into tap water. After removing the bubbles, this solution was transferred to the test section as second layer.
3. Experimental tank (test section) was sealed using screws.
4. Set up was left for few hours to get the interface layer horizontal.
5. The camera is focused on the test section with an optimal zoom.
6. The laser is turned on and the laser sheet is carefully set to the required position.
7. All external lights are switched off and the experiment is started by inverting the setup.
8. Camera is turned on and images are captured.

9. Eleven equidistant vertical planes have been captured with time in order to study the phenomena in full domain. This was done by sliding the laser and optics setup manually on a square cross section rod as described earlier.

3.11 Experimental details

As mentioned before, in the experiments, the convection is driven by compositional buoyancy resulting from a concentration difference across the upper layer and bottom layer. The analogy that has been used here is between heat transfer and mass transfer phenomena. The thermal Rayleigh number (Ra_T) has been modified to define a compositional Rayleigh number, (Ra_c) as

$$Ra_T = \frac{g\beta_T \Delta T H^3}{\nu\alpha} \quad \rightarrow \quad Ra_c = \frac{g\frac{\Delta\rho}{\rho}H^3}{\nu\alpha_m}$$

The Schmidt Number (Sc) is the proxy for Prandtl Number (Pr):

$$P_r = \frac{\nu}{\alpha} \quad \rightarrow \quad Sc = \frac{\nu}{\alpha_m}$$

Here, g = acceleration due to gravity, β_T = coefficient of thermal expansion, ΔT = temperature difference between the walls, H = height of the fluid layer, ν = kinematic viscosity, α = thermal diffusivity of the fluid, $\Delta\rho$ = density difference between the bottom layer fluid and overlying fluid.

ρ = density of the bottom fluid, α_m = mass diffusivity of sugar in viscous water.

3.12 Convective diapiric structures and analysis

Our objective is to study the effect of viscosity, thickness ratio and density difference between top and bottom layer on diapiric structure formation i.e. how number of structures, their thickness and average spacing between them vary with these parameters (Pr, Sc, Ra and thickness ratio). Results and analysis obtained from our experiments are reported here.

Twelve experiments were conducted for different values of viscosity, density difference and layer thickness ratios. All the experiments were carried out for very high viscous solution at room temperature. Details of these parameters are shown in table 3.1.

Experiments # 1-3 have been conducted with 120 gm/cc^3 density difference, 2.5% CMC solution for both the layers and three different layer thickness ratios (1/9, 1/4 and 2/3). Experiments # 4-6 and 7-9 are conducted for 3.0% CMC and 3.5 % CMC with above thickness ratios and density contrast. Similarly other three experiments were conducted for 80 gm/cc3, three different layer thickness ratios (1/9, 1/4 and 2/3) and 3.5% CMC solution.

As all of our experiments were conducted with very high viscous solutions, we could not observe any changes in the diapir structure for variation in density contrast. So all the results in this thesis are restricted to viscosity and layer thickness ratio variation. For all these cases initially we observed a particular characteristic wavelength. As system runs down with time, these wavelengths were changed and were varied for different section of the experimental domain because of merging and splitting of plume structures. Figure 3.9 shows the evolution of diapir like structures, that has been generated first time in our laboratory. For this experiment 3.5% CMC solution and layer thickness ratio of 2:3 has been used. The time taken from stage 1 (first picture) to stage 2 (last picture) in figure 3.9 was approximately 5 hours. This experiment was conducted when the bubble removing setup was not fabricated.

3.12.1 Layer thickness effect on diapirs like structure

To study the layer thickness effect, experiments for three different layer thickness ratios (TR = 1/9, 1/4, 2/3), two different density contrast ($\Delta\rho - 120$ and 80 gm/cm3) and for solutions of three different viscosities (2.5, 3 and 3.5% CMC) have been conducted.

Experiment No.	CMC %wt	Density diff. (gm/cm^3)	Layer thickness ratio (TR)
1	2.5	120	1/9
2	2.5	120	1/4
3	2.5	120	2/3
4	3.0	120	1/9
5	3.0	120	1/4
6	3.0	120	2/3
7	3.5	120	1/9
8	3.5	120	1/4
9	3.5	120	2/3
10	3.5	80	1/9
11	3.5	80	1/4
12	3.5	80	2/3

Table 3.1: A list of all the experiments and their parameters

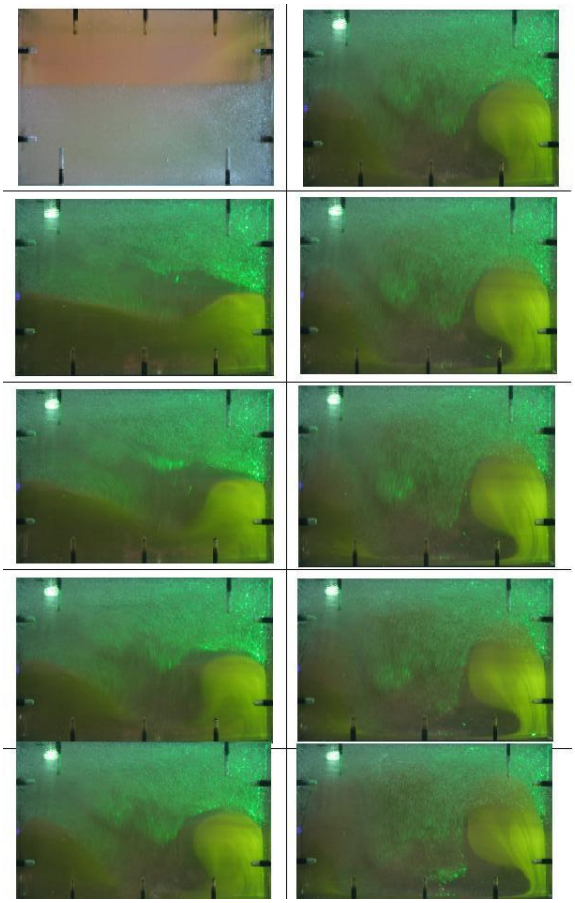

Figure 3.9: Evolution of salt-diapir like structures in laboratory

(a) Layer thickness ratio (TR) =1:4

In this section, a particular case in which a layer thickness ratio of 1:4 i.e., the dense bottom layer is of 4 cm height and remaining 16 cm is filled with lighter solution, has been explained in detail. Eleven vertical planes using the traverse mechanism and experimental procedure described previously have been captured. Figure 3.10 shows raw images of the evolution of these structures. For simplicity only six planes have been shown here. Six columns shown here are six vertical planes of experimental tank. Each row depicts evolution of these structures, with time. In the first row, pictures were taken at t=0 for all six planes. 2nd row shows all the pictures, were taken after 10 minutes. 3rd row at t=16 minute and in the last row pictures were taken after 30 minutes.

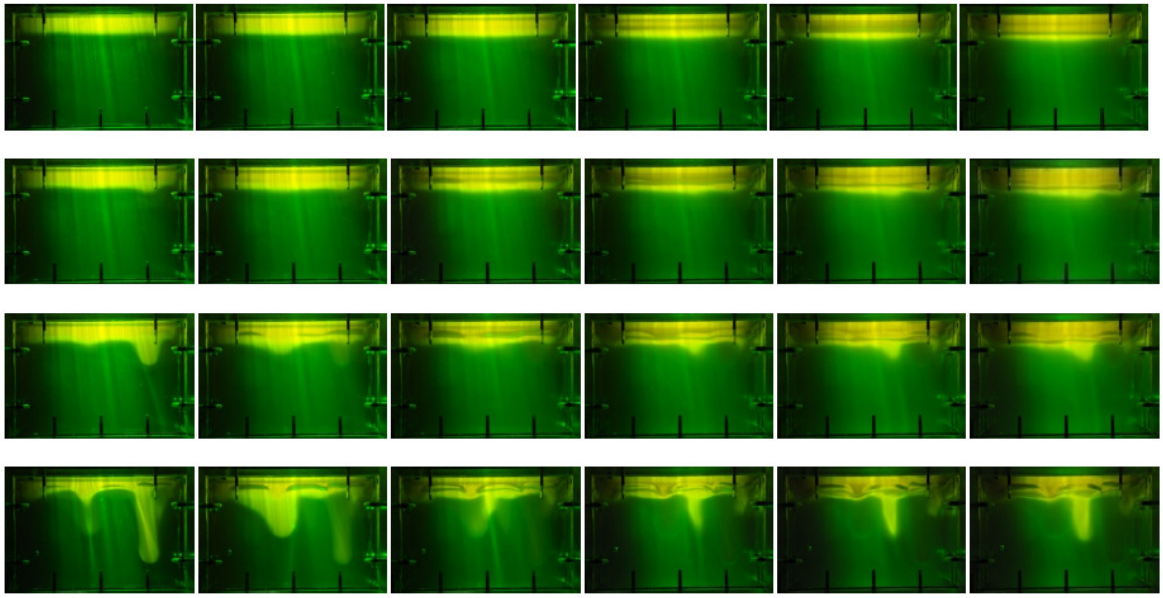

Figure 3.10 Time sequence of six vertical planes showing the evolution of concentration field in six planes

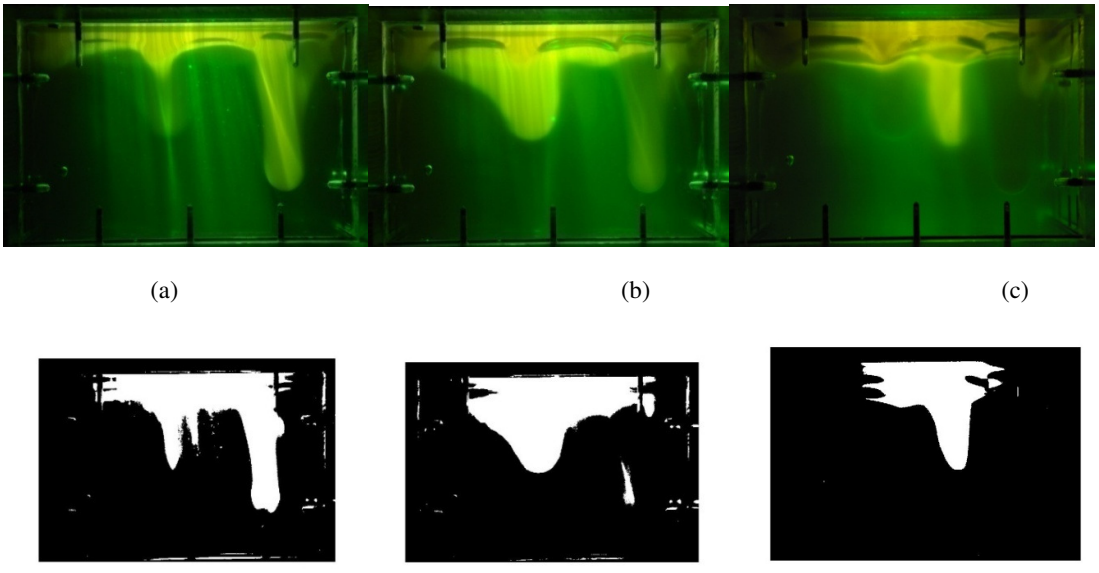

Figure 3.11 Raw images of Diapiric structures (a,b,c) and corresponding Matlab processed binary images(d,e,f).

In figure 3.11, the only planes where diapirs were detected are shown. At a depth of 5 cm (figure 3.11a) from rear wall, we observed a plume structure at a distance of 23.6 cm from left corner. Second structure was observed at a depth of 7.5 cm (figure 3.11b) from rear wall and 13.77 cm from left corner. The last plume was observed at a depth of 17.5 cm (figure 3.11c) and at a distance of 18 cm from left wall. All the image processing and analysis is done in Matlab. First all the images were converted into grayscale and then they were combined together to get 3D picture as shown in figure 3.12.

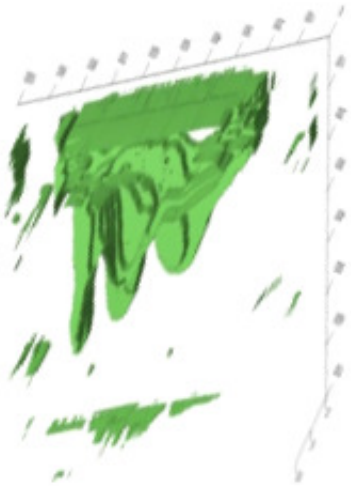

Figure 3.12: 3D diapiric structure for TR = 1:4

In the table given below (table 3.1), the height of diapiric structures with time has been tabulated. The position and average thickness have also been located. In figure 3.13, the location i.e. coordinates in horizontal plane and their thickness has been depicted. Figure 3.14 shows how their heights vary with time. From this plot we will be predicting the evolution of geological salt-diapirs, their growth and velocity in geological time scale.

No.	Time (minutes)	Structure1 Location: 3rd from wall (in pixels)	Structure2 Location :4rd from wall (in pixels)	Structure3 Location :8rd from wall (in pixels)
1	0	0	0	0
2	5	0	0	0
3	11	100	0	20
4	14	330	200	20
5	16	530	300	250
6	19	780	420	580
7	23	1200	720	820
8	27	1530	930	980
9	30	1850	1290	1200

Table.3.2: Location of diapiric structures and evolution of height with time

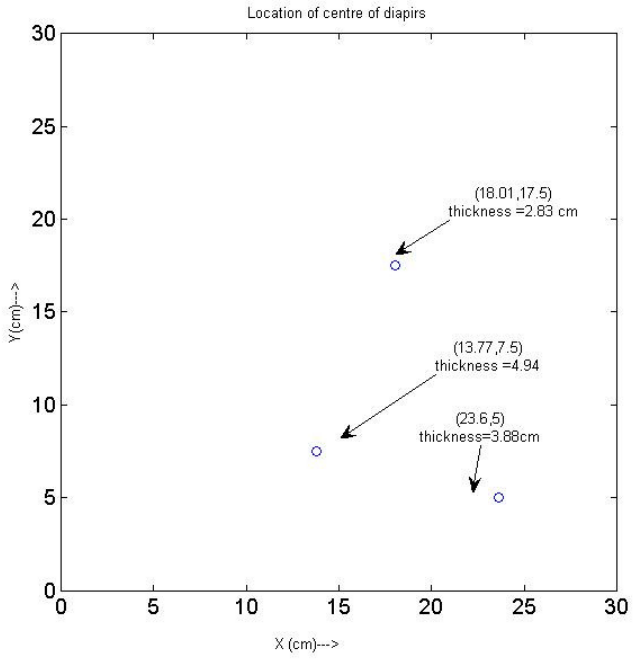

Figure 3.13: Location and thickness of diapiric structures in the experimental tank

Thickness range (diameter): 2.5 cm to 5 cm

Spacing range: 10cm to 14 cm (10.143cm, 10.86cm and 13.69cm)

Number of diapirs =3

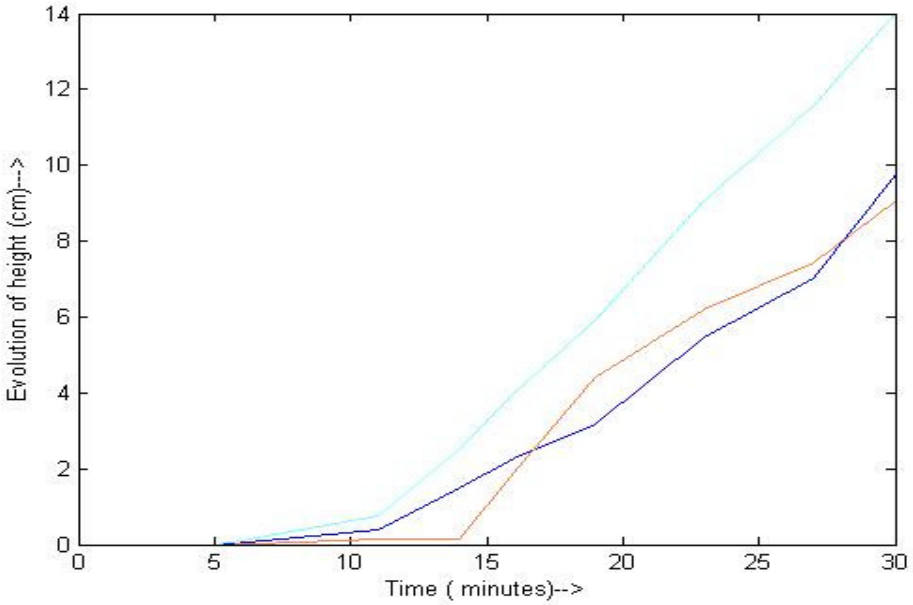

Figure 3.14 Height of diapiric structures as a function of time

(b) Layer thickness ratio (TR) = 2:3

In this case, layer thickness ratio 2:3 i.e. the dense bottom layer is of 8 cm height and remaining 12 cm is filled with lighter solution. Eleven vertical planes have been captured using the traverse mechanism and experimental procedure described previously. Figure 3.15 shows the evolution of these structures and figure 3.16 shows 3D Matlab processed image of that.

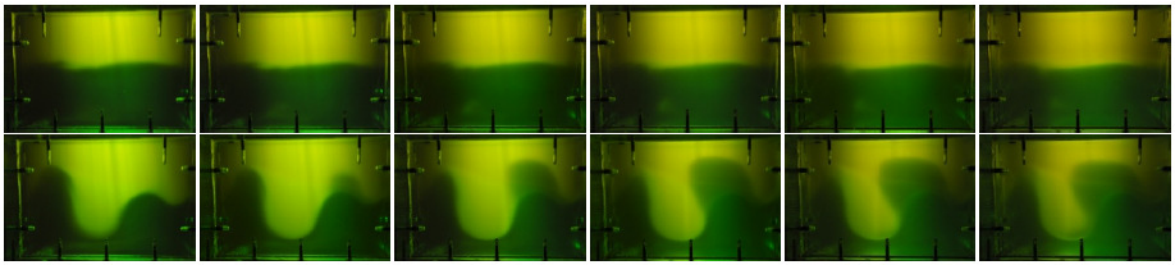

Figure 3.15: Diapiric structure formation for layer thickness ratio 2/3. Six columns are six different vertical cross-section of the experimental tank. First row is captured at t= 2 minute and second row at t = 8 minute.

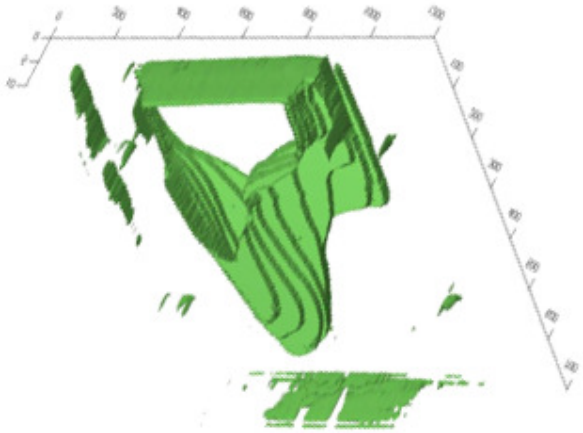

Figure 3.16 3D image for the case of TR = 2/3.

(c) Layer thickness ratio (TR) = 1:9

In this case, layer thickness ratio 1:9 i.e. the dense bottom layer is of 2 cm height and remaining 18 cm is filled with lighter solution. In the same way eleven vertical planes have been captured using the traverse mechanism and experimental procedure described previously. Figure 3.17 shows the evolution of these structures.

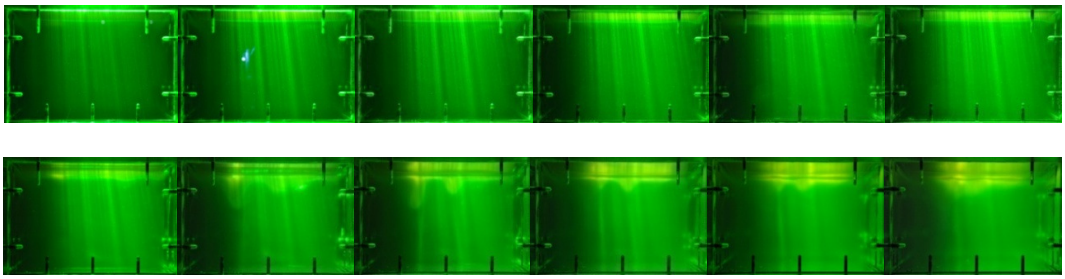

Figure 3.17 Diapiric structure formations for layer thickness ratio 1/9. Six columns are six selected vertical cross-sections where these structures were detected. The pictures in the first row were captured at t=0 minute and in the second row at t = 38 minutes.

3D formation by image processing for this case was not possible because of very thin structures formation. It would be possible if we were able to capture vertical planes with very small gaps. For that very fine traverse arrangement would be required. In this case the lengths and coordinates have been measured by reading them directly in Matlab.

3.12.2 Viscosity effect on diapiric structures

(a) 3.5% CMC solution

In this case the layer thickness ratio 1:9 and 3.5% CMC solution have been used. Figure 3.18 shows the evolution of these structures and Figure 3.19 shows 3D form of this case.

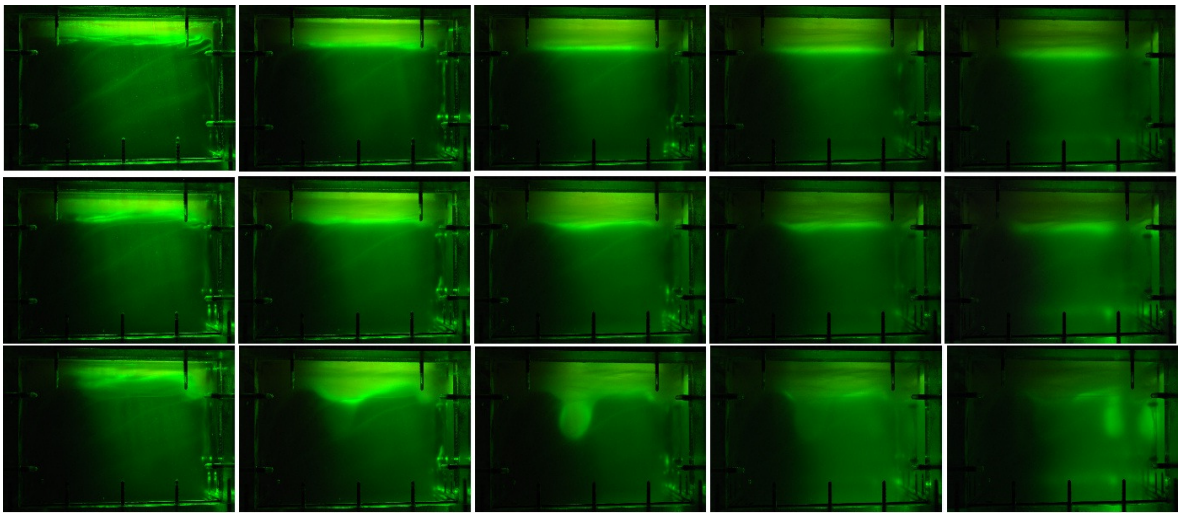

Figure 3.18: Evolution of diapiric structures with time for 3.5%CMC solution. Five columns are five vertical cross-sections of experimental tank. First row is at t = 0, second row at t = 68 and third row at t = 116 minutes.

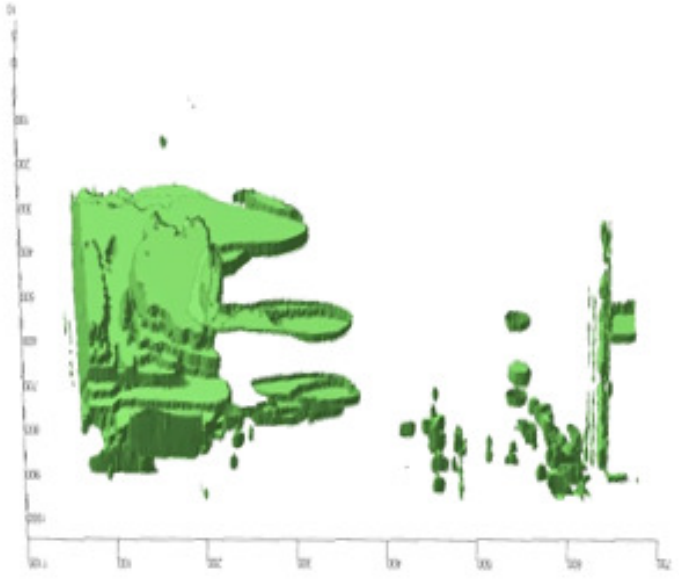

Figure 3.19: 3D diapiric structure of 3.5% CMC case

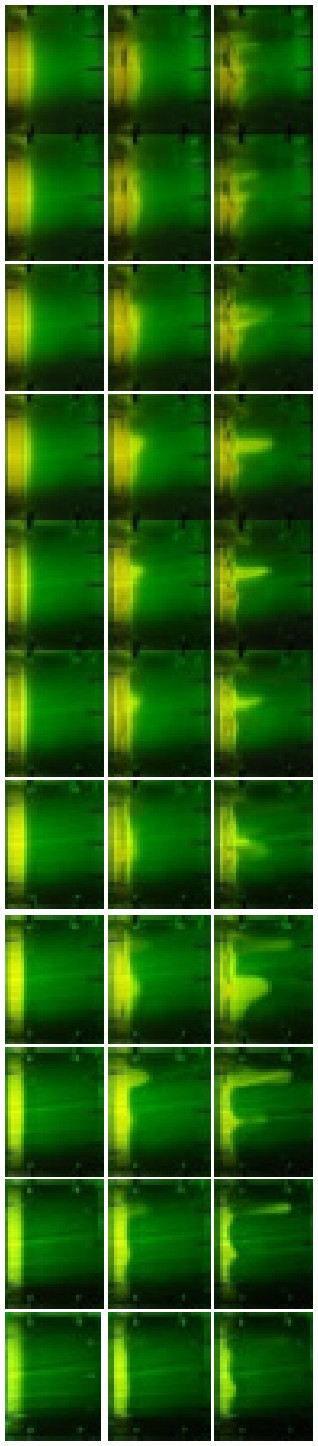

Figure 3.20: Time evolution of diapiric structures for 3% CMC solution. First row at t=0, second row t=16 minute and third row at t=27 minutes. Eleven columns are eleven vertical cross-sections of experimental tank.

(b) 3% CMC solution

This case has been explained in detail in our previous study [see § 3.12.1a] Figure 3.20.

(c) 2.5% CMC solution

For less viscous cases instead of cylindrical shape, sheet kinds of structures were found. The reason is less viscosity of the fluid. These structures do not simulate salt diapirs so the analysis for such cases have not been done.

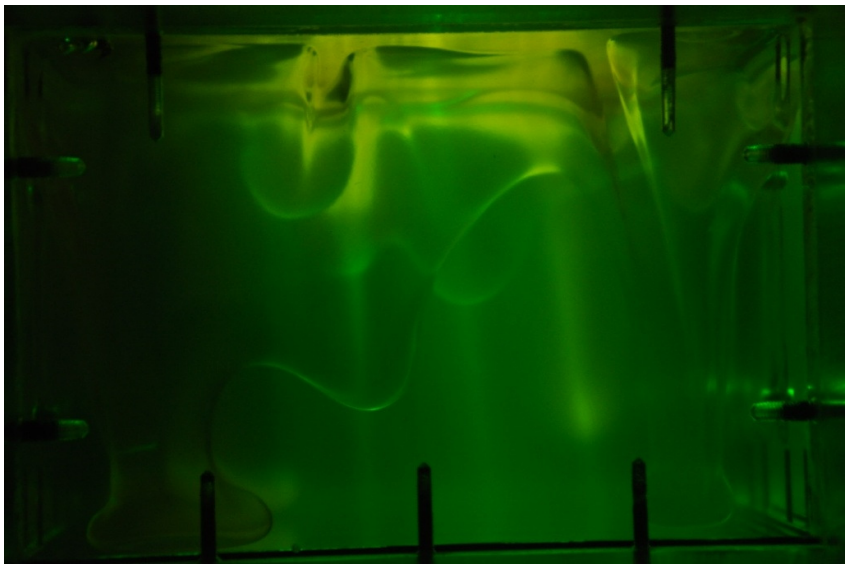

Figure 3.21: Experiments with less viscous fluid (2.5% CMC ~ $5.0X10^5$ mPa-s)

So far changes in diapiric structures qualitatively have been described. In later chapters the approaches that have been used for a quantitative analysis of plume spacing and thickness for different cases of viscosity and layer thickness ratios will be described. To analyze this, codes in Matlab has been written to read and post process the selected images.

Chapter 4

Results and Analysis

In this chapter, the data extracted from simulation and experiments have been analyzed. Our objective is to study the dynamics of salt-diapirs. Some of the results from simulations have been verified quantitatively from experiments.

4.1 Simulation results

The simulations have been carried out by varying the layer thickness ratio, Sc number and Gr number. The effect of these parameters on length scale (spacing, thickness) and velocity in the diapirs is studied by means of the evolution of kinetic energy of the system and.

4.1.1 Effect on average spacing and thickness

(a) Effect of Gr number

To study the effect of Gr number variation, Sc number and layer thickness ratio have been kept constant. At constant mass diffusivity, constant Sc number ($Sc = \frac{\nu}{k_s}$) implies that viscosity is constant. So the study that has been done for Gr number variation with constant Sc number and layer thickness ratio is the effect of density difference variations between two layers. It has been observed that length scale (spacing between two diapiric structures or their thickness) do not vary rapidly for these small changes in Gr number [see figure 2.4]. The reason for this is explained below.

Sreenivas K. R. et al. (2009) showed that non-dimensional finger width of the incipient fingers at the time of onset of instability vary as $Ra^{-1/3}$.

$$Ra = Gr.\ Sc$$

So at constant Sc number, width will be proportional to $Gr^{-1/3}$.

The change in the width of diapiric structure, when Gr number is changed from 40000 to 5000 has been calculated as 0.93 times. The small variation in Gr number at constant Sc number will cause a very small change in the thickness of diapiric structures. These changes are not apparent in figure 2.4a to figure 2.4f as figures look similar [see § 2.3.2]. For these small variations in Gr number, the changes could be visualized in the time taken to develop the diapiric structures upto same height or in the dynamics of diapirs. In these small variations it could be observed that as Gr number is increased, the time taken to develop these diapiric structures upto same height is reduced.

Gr number	**Number of diapirs**	**Avg Spacing (cm)**	**Avg Thickness (cm)**
10^5	5	6	3.6
10^6	7	4.2	3
10^7	12	2.5	2.4
10^8	18	1.66	1.3
10^9	32	1.01	0.9

Table 4.1: Variation in number of structures, average spacing and average thickness with Gr number

In table 4.1 the average spacing, thickness and number of diapirs have been shown for different Gr numbers. Significantly large changes in Gr number will cause noticeable changes

in the length scale. These changes could be seen in figure 2.5, [see §2.3.2] in number of diapiric structures, thickness and spacing. Using Matlab, data extracted from simulation has been analyzed and following parameters have been measured for different Gr number. 100X100 grid size has been scaled to simulate 30cmX20cm experimental 2D tank.

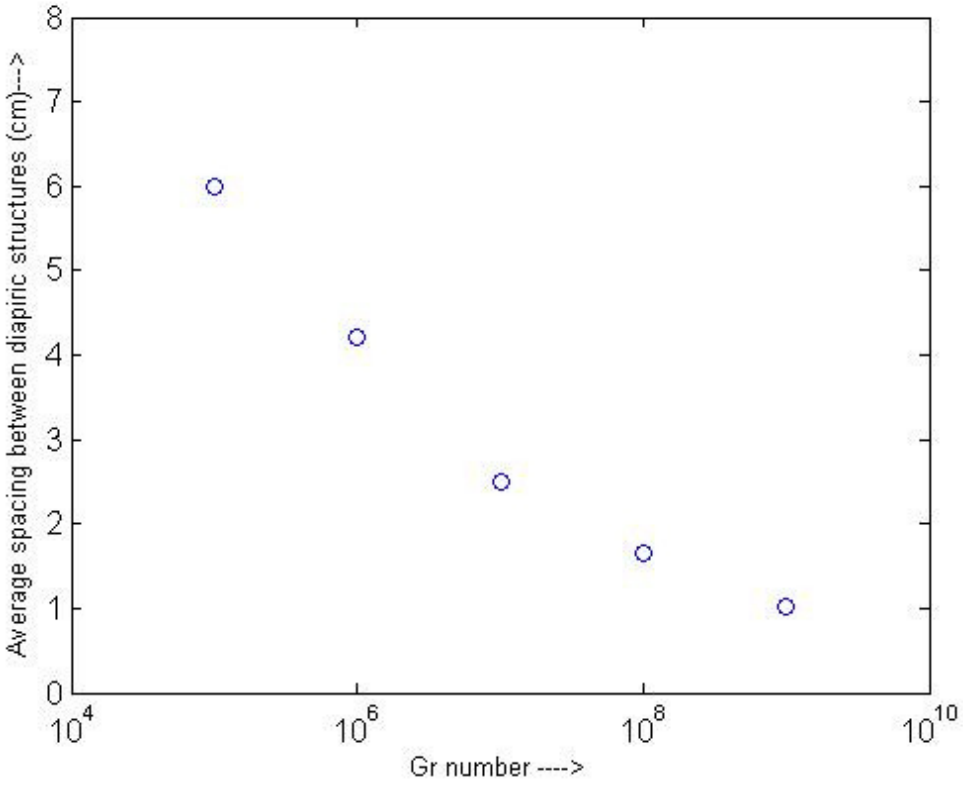

Figure 4.1 Variation of average spacing between diapirs with Gr number at constant Sc number (1000) and layer thickness ratio (1/19)

Figure 4.1 shows the variation of average spacing between diapirs as a function of Gr number. As it was expected it is observed that this spacing decreases with Gr number or in other words we can say that the number of diapirs increases with Gr. As these simulations are carried out at constant Sc number, for high Gr numbers (or high density contrast) gravity forces will be higher. Because of gravity forces, vertical velocity will be larger in comparison

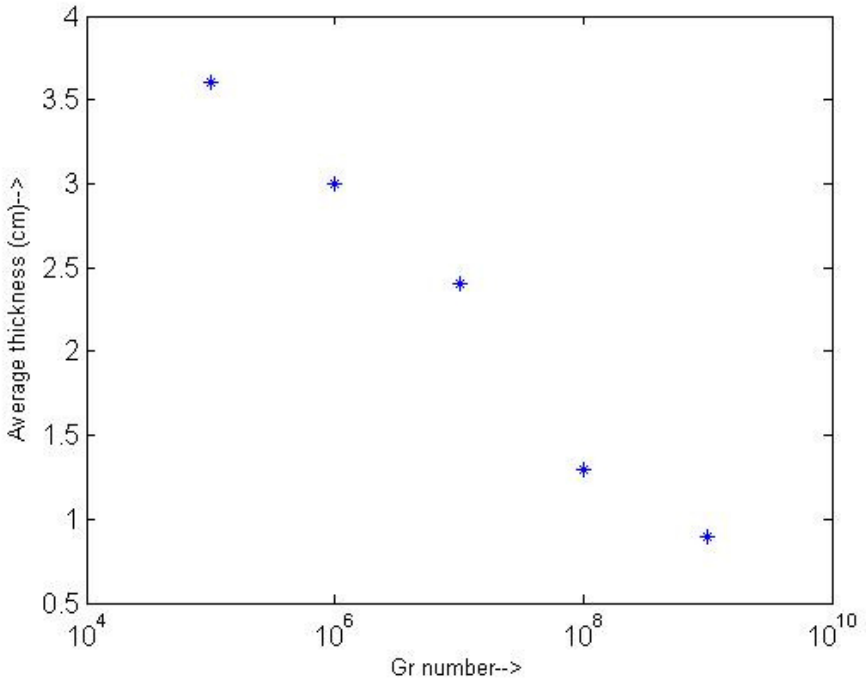

Figure 4.2 Variation of average thickness of diapirs with Gr number at constant Sc number (1000) and layer thickness ratio (1/19)

to smaller Gr number. This larger vertical velocity will cause mass to move faster in vertical direction and the width of diapirs (and spacing) will be reduced. This decrease in thickness of diapirs will cause decrease in spacing between diapirs [see figure 4.2]. It means wavelength of instability will become smaller if Gr number is increased.

(b) Effect of layer thickness ratio (TR)

To study the effect of layer thickness ratio on the dynamics of diapirc structures, Gr number and Sc number has been kept constant (Gr=40000, Sc=1000) and layer thickness ratio has been varied. Spacing between diapirs increases as layer thickness ratio is increased to one and as Tr is increased beyond one, number of structures again start decreasing. Same information has been observed for thickness also. The reason for this behavior is the similar boundary conditions that have been used for upper and lower walls i.e. symmetry.

Layer thickness ratio	Number of diapirs	Avg Spacing (cm)	Avg Thickness (cm)
1/19	5	5.8	2.85
3/17	3	9	3.6
5/15	2.5	12	4.5
7/13	2	15	6
11/9	2	15	6

Table 4.2: number of structures, average spacing and thickness with Gr number

In table 4.2 average spacing, thickness and number of diapirs have been shown for different layer thickness ratios and have been plotted in figure 4.3 and 4.4.

In the case of layer thickness ratio variation, for very small thickness ratio and an early stage of development, two different length scales were found but as this thickness ratio tends to one, thickness and spacing were observed to be of approximately same length. In other word contour plot of concentration is very similar to sinusoidal curve as these thickness ratios tends to one. At later time of their evolution because of merging and splitting they became two

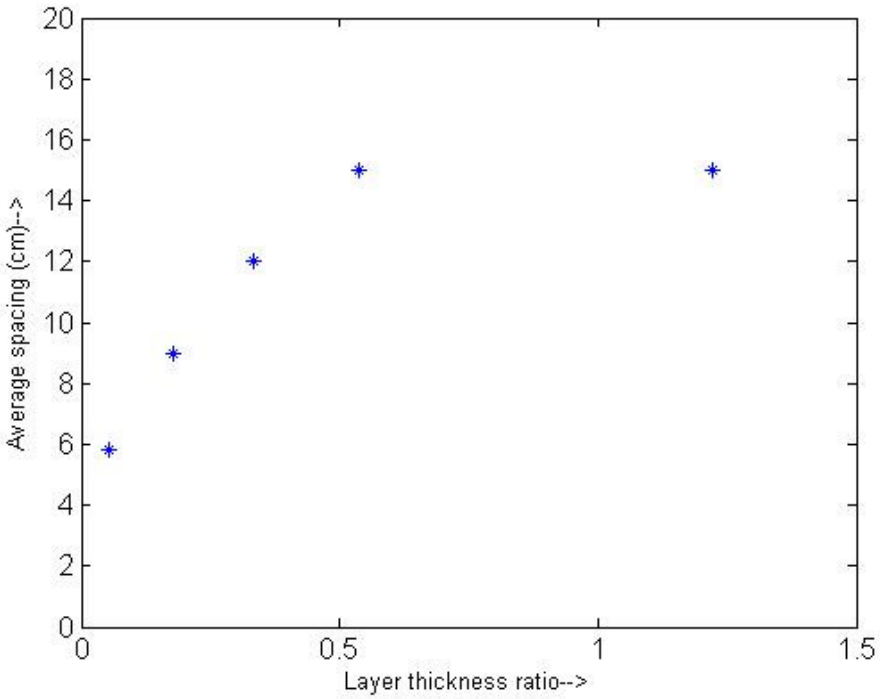

Figure 4.3: Variation of spacing between diapiric structures with layer thickness ratios for Gr number 40000

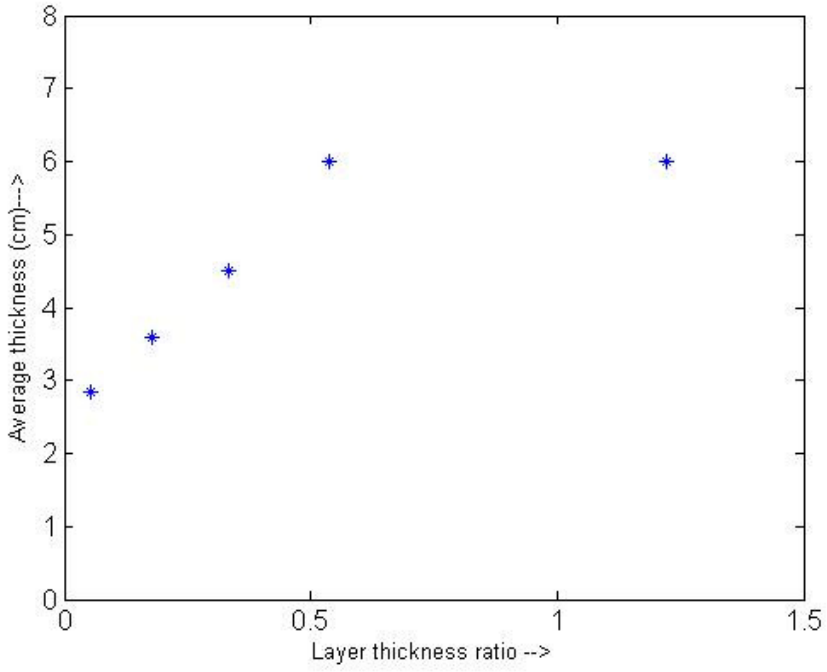

Figure 4.4: Variation of average thickness of diapiric structures with layer thickness ratios for Gr number 40000

length scales (spacing and thickness). It has been observed here that wavelength of instability is strongly dependent of layer thickness ratio and increases as layer thickness ratio increases.

(c) Effect of Sc number

Sc number variations do not cause any significant changes in diapiric structures as have been shown in § 2.3.3. Sc number effect could be seen on the dynamics of diapirs. In figure 4.7 non-dimensional kinetic energy have been shown for two different Sc numbers (10^4 and 10^9) with thickness ratio, TR = 1/19 and Gr =10^4 [see § 4.1.2 (d)].

4.1.2 Effect on kinetic energy

Kinetic energy is a measure of the velocity of the diapirs. Here velocities of diapiric structures have been interpreted in terms of kinetic energy as velocity is proportional to square root of K.E. Velocity plays a crucial role in transporting heat and salt flux vertically. The non dimensional kinetic energy is calculated as

$$E_k = \frac{1}{2}\langle u^2 + v^2 \rangle$$

Note how the kinetic energy (E_k) of the system varies in all the cases [see figure 4.5, 4.6 and 4.7]. Initially, for certain period of time $E_k \approx 0$, then E_k starts increasing, reaches a maximum value and then tends towards zero. The time upto which $E_k \approx 0$ is the onset time of convection. During this period the system is dominated by molecular diffusion and no instability develops at the interface. We define onset of convection (t_0) as the time when kinetic energy rises above 2% of the maximum kinetic energy ($E_{k,max}$).

(a) Effect of Gr number

In figure 4.5 non-dimensional kinetic energy as function of non-dimensional time has been plotted for three different Gr numbers [10^8,10^6 and 10^4] at thickness ratio 1/19 and Sc number 1000. It can be observed from the figure that with the decrease in Gr number, onset time

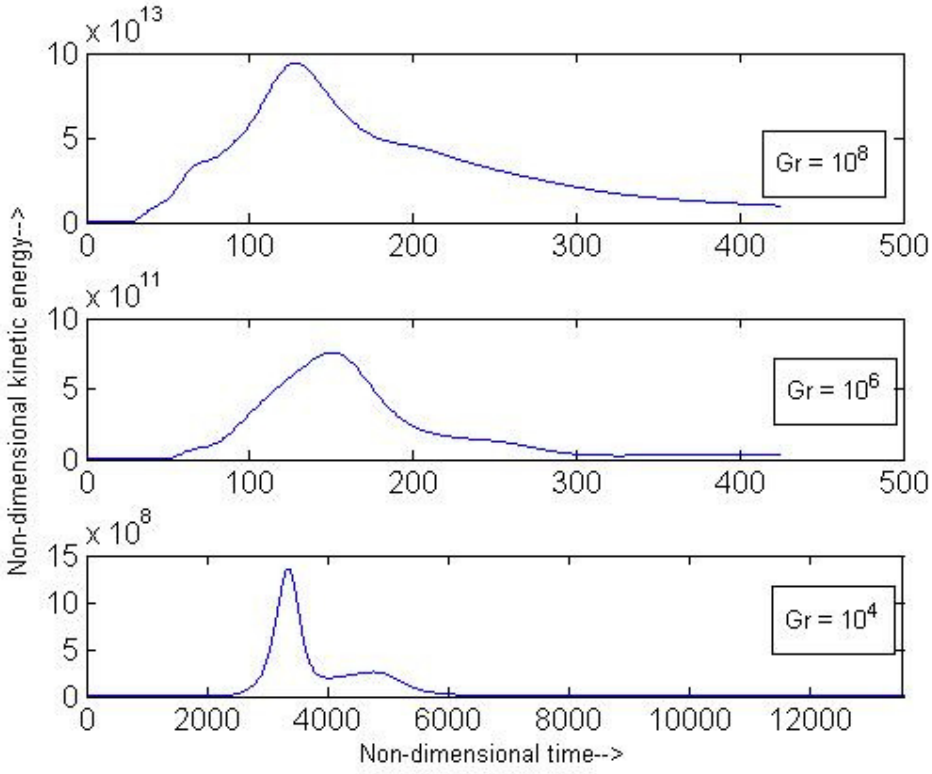

Figure 4.5: Evolution of kinetic energy at Sc = 10000 and Tr=1/19.

increases and the value of maximum kinetic energy decreases. We have also calculated and concluded the growth rate of kinetic energy just after the onset time and observed that, growth rate of kinetic energy doubles if Gr number is increased two times.

(b) Effect of layer thickness ratio

In figure 4.6 non-dimensional kinetic energy as function of non-dimensional time has been plotted for two different layer thickness ratios [3/17 and 1/19] at Gr number 10^5 and Sc number 1000. It can be observed from the figure that with the decrease in layer thickness ratio, onset time increases and the value of maximum kinetic energy decreases.

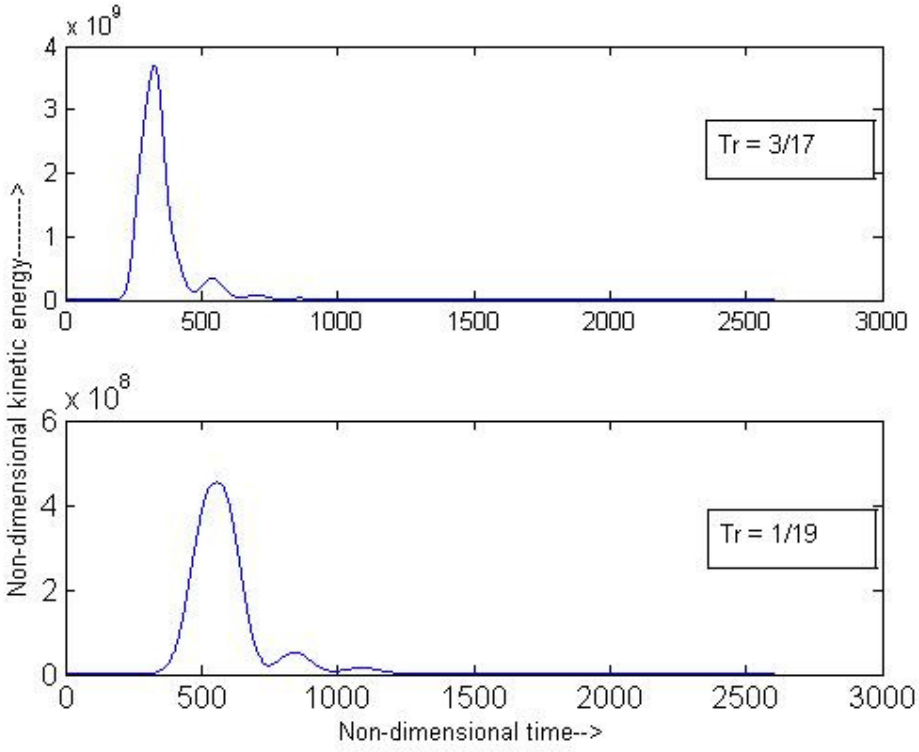

Figure 4.6: Evolution of kinetic energy at Sc = 1000 and Gr = 10^5

(c) Effect of Sc number

In figure 4.7 non-dimensional kinetic energy as function of non-dimensional time has been plotted for two different Sc numbers [10^9 and 10^4] at thickness ratio 1/19 and Gr number 10000. It can be observed from the figure that with the increase in Sc numbers, onset time increases [see figure 4.7, with increase in Sc number from 10^4 to 10^9, the non-dimensional onset time is increased from 500 to 2500] and the value of maximum kinetic energy decreases. As Sc number is proportional to viscosity the possible explanation for this may be that as Sc number is increased, viscosity of the fluid increases and that will reduce the rate of convection or mixing. This will cause to slow down the phenomenon as onset time will be higher when Sc number is increased.

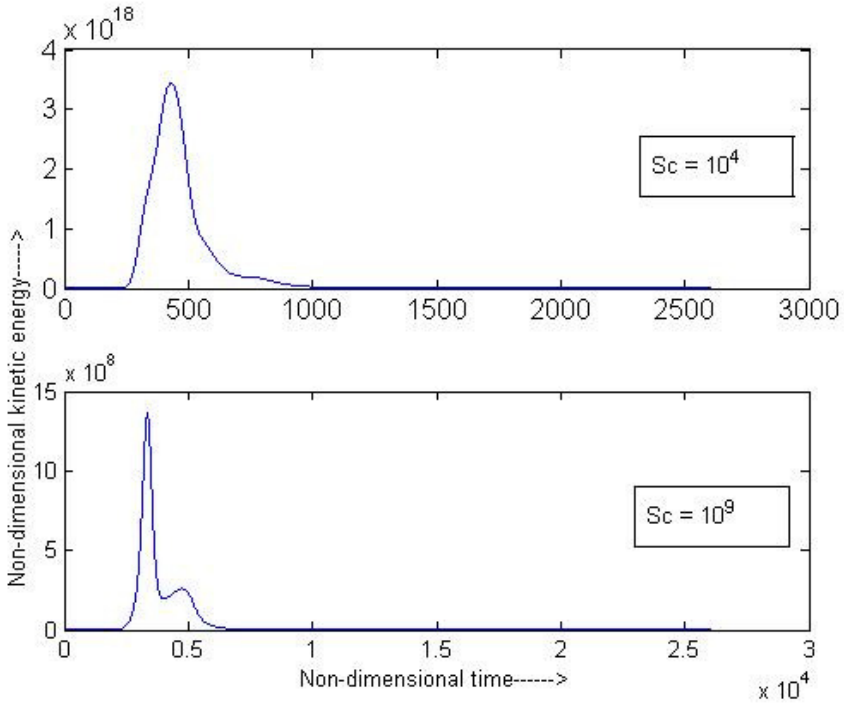

Figure 4.7: Effect of Sc number [Gr=10^4 and TR = 1/19]

4.2 Experimental results and comparison with simulations

Some results extracted from experiments have been produced here. In the experiments layer thickness ratio, fluid viscosity and density contrast have been varied and their effect on diapiric structures has been studied and the results from layer thickness ratio variation at constant Rayleigh number have been verified with simulation.

4.2.1 Effect of layer thickness ratio

In this section the results from three experiments have been shown for three different layer thickness ratios (TR = 1/9, 1/4, 2/3) with same fluid viscosity (3%CMC or 1.5X10^6 mPa-S, see figure 3.7) and density contrast (120 gm/cm^3). Ra number for this case has been calculated as 1.4X10^7.

Layer thickness ratio (TR)	1/9	1/4	2/3
No. of diapirs	4	3	1
Avg spacing	7.1 cm	11.56 cm	15 cm
Avg thickness	2.32 cm	3.75 cm	11 cm

Table 4.4: Variation of the diapirs parameters with layer thickness ratio

From the simulation, a case with Gr = 40000 and Sc = 1000 has been taken. For this case Ra = Gr.Sc = $4X10^7$. The results of this simulation have been verified from the experiments described above for layer thickness ratio variations, as experiments and simulations are in the same order.

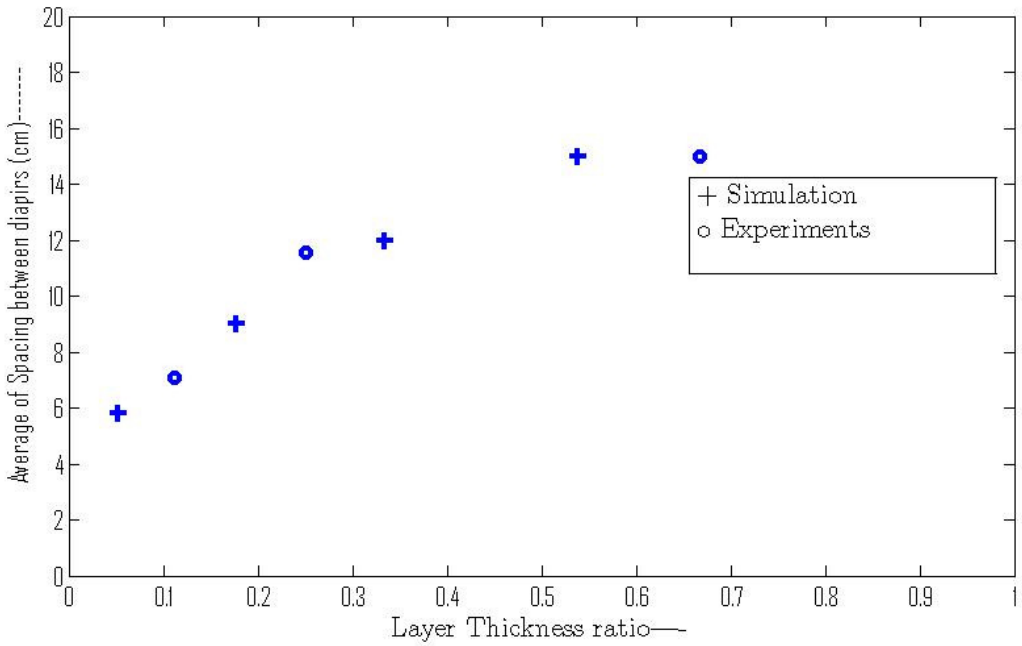

Figure 4.8: Variation of average spacing with layer thickness ratio. '*' values are from experiments and '+' from simulations.

From figure 4.8 and 4.9 it can be observed that average spacing and thickness, extracted from simulation and experiments, behave in the same manner at same Rayleigh number.

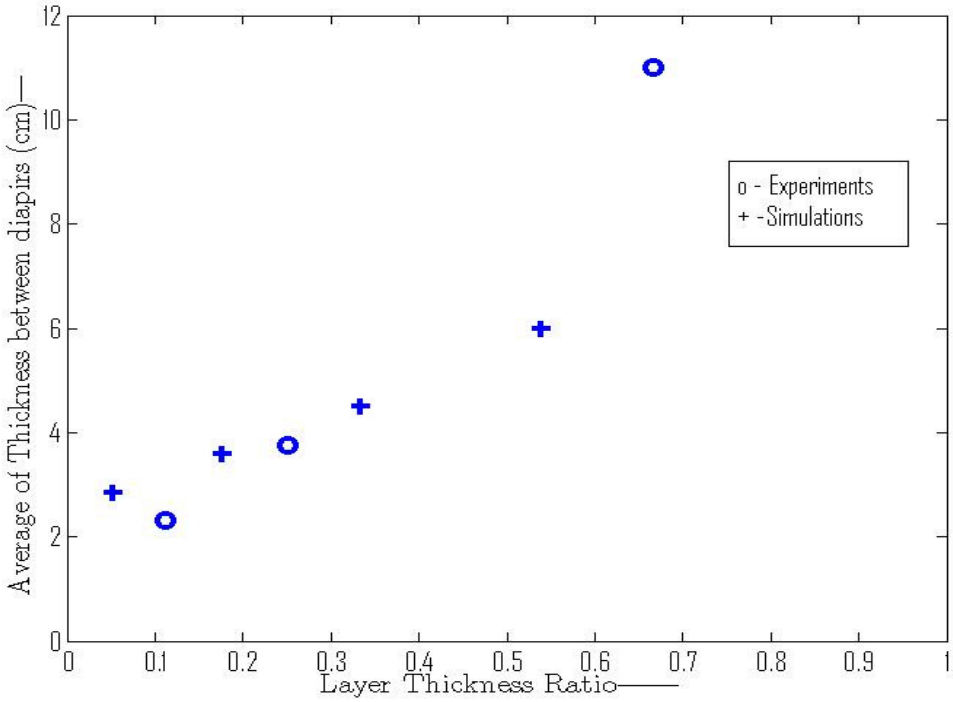

Figure 4.9: Variation of average thickness with layer thickness ratio. ['*' values are from experiments and '+' from simulations.]

Because of various limitations in the experimental setup, it is not possible to compare all the simulation results from experiments. These experimental results for the variation in layer thickness ratio show quantitative verification of simulation. The results obtained from simulation and experiments for spacing (or number of diapiric structures) and thickness of diapirs is in good agreement. On the basis of these conformities the dynamics of salt-diapirs has been predicted from the results extracted from simulations. The introduction of strongly non-Newtonian rheology may greatly affects instability parameters such as growth rate and dominant wavelength of perturbations and hence, may alter inter-diapir spacing.

4.3 Dynamics of Salt-diapirs

From the results of our study, we correlate some of the important features that are relevant in anticipating the dynamics of salt-diapirs. With the help of a simple model, we have shown that growth rates and wavelength are function of a number of properties of the fluids.

In our results we have shown that the wavelength of salt-diapir structures is controlled by density difference, viscosity and layer thickness ratios of salt diapirs. Salt-diapir seems to be spaced at a characteristic wavelength.

The dominating influence on wavelength is the thickness of layers. Increasing the overburden thickness invariably increases the characteristic wavelength and takes comparatively lesser time to develop the diapirs upto same height as the growth rate will be higher [see § 4.1.2 (b)]. It has been observed that as thickness ratio tends to one [TR=1], we will get only one length scale i.e. thickness and spacing will be of same order. For very small thickness ratios [TR = 1/19], two different length scales [thickness and spacing] were observed.

As the viscosity of salt layer increases, the rate of deformation slows down. The growth rate of the instability depends inversely on viscosity.

Density contrasts have little effect on wavelength, but a large contrast across the interface to the buoyant layer accelerates the growth rate. It has been shown that growth rate doubles if density difference is increased by a factor of two.

4.4 Predicting the spacing and width of salt-diapir

Here we are trying to predict the spacing of salt-diapirs and their thickness from the results we have obtained. In the previous chapter, the variation of spacing and thickness of diapiric structures, obtained from our study [see § 4.2.1, figure 4.8 and 4.9] were shown. Assuming a linear profile, the variation in thickness and spacing with thickness ratio (TR) has been interpolated and shown here.

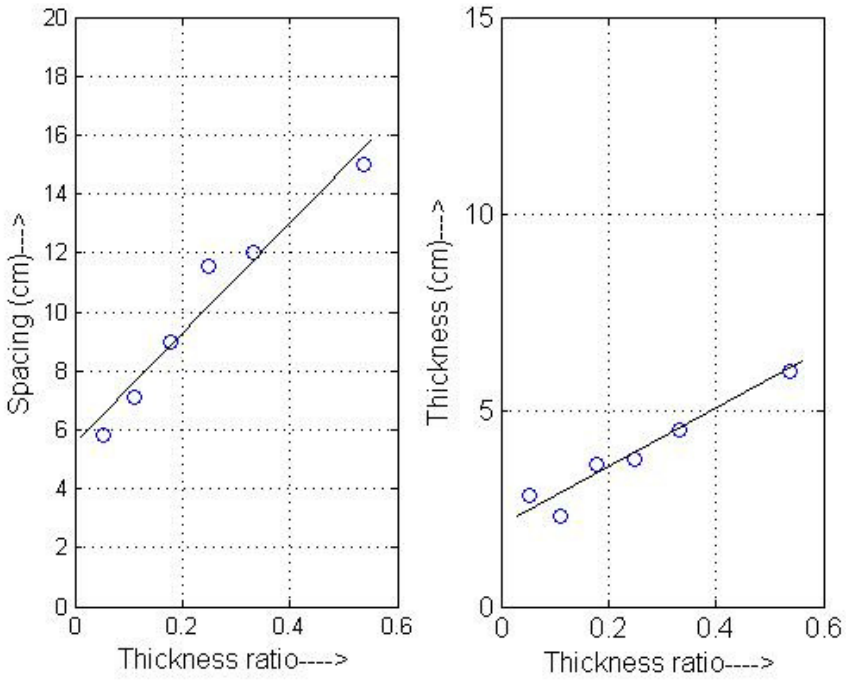

Figure 4.10: Spacing and thickness of diapiric structures extracted from our study for Ra $\approx 10^7$.

If we imagine that a geological site of diapiric clusters in a large area of length 30 km had 1 km thick salt layers deposited under the sediments of 4 km above it before the development of these structures, then:

Thickness ratio = 1/4 = 0.25;

Spacing (d1) = 10.5 cm (figure 4.1)

Thickness (t1) = 3.8 cm (figure 4.1)

Average thickness of diapirs in that geological site

$$= \frac{\text{t1}}{\text{experimental domain}} \text{ X Geological domain}$$

$$= \frac{3.8cm}{30cm} \text{ X 30km} = 3.8 \text{ km}$$

Average spacing of diapirs in the geological site

$$= \frac{d1}{experimental\ domain}\ X\ Geological\ domain$$

$$= \frac{10.5cm}{30cm} \text{ X } 30\text{km} = 10.5 \text{ km}$$

Note that these calculations have been done for Ra= 10^7. The spacing and thickness of salt-diapirs will vary with Ra number. The viscosity of salt layers in the Gulf of Mexico has been measured in the order of 10^{17} pa-s. If we take the density of sediments 2.8 gm/cm^3 and of salt 2.2 gm/cm^3 [see Jackson and Seni, 1984] buried at the depth of 4 km and mass diffusivity in the order of 10^{-10} m^2/s, the Ra number for this case will also be in the order of 10^7.

In various geological locations the salt dipairs thickness and their spacing have been found of the same order.

Chapter 5

Conclusions and Future Outlook

The main objective of this work was to study the dependency of Rayleigh Taylor instability on parameters like density difference, viscosity and layer thickness ratio and to predict the dynamics of salt-diapirs. We conducted experiments in a glass tank of square cross-section. A simple traverse setup that enables the movement of a vertical laser sheet in the horizontal direction is used to visualize the structures in 3D. A non-intrusive Planar-Laser-Induced-Fluorescence (PLIF) technique has been used in which a water-soluble fluorescent dye is used as a scalar flow marker. All the experiments were carried out for very high viscous solution at room temperature. The changes in diapirs spacing and thickness with above parameters have been quantified using image processing techniques. For all the experiments initially we observed a particular characteristic wavelength. As system runs down with time, these wavelengths were changed and were varied for different section of the experimental domain because of merging and splitting of plume structures. Simulations were carried out to study the physics behind the formation of salt-diapirs and their dependency on non-dimensional parameters like Gr number, Sc number and layer thickness ratios. For our study we have considered negligible effect of temperature. Some of the simulation results are comparable with experimental results as discussed in previous chapter.

From experiments the actual physics that govern the cluster formation of salt-diapirs and how above parameters are related to diapirs width and spacing is explored. It has been observed from experiments that as the layer thickness ratio (Tr) increases the diapirs width and spacing between them also increases. In other word we can say that wavelength increase as layer

thickness ratio tends to one. Average of thickness and spacing between neighboring diapirs were found to be decreasing as Gr number increases.

The viscosity of solution is improved by adding CMC to water. With increase in viscosity the resisting force against buoyancy increases so the system tends to be stable. The width of diapirs increases at a slower rate with increase in viscosity.

From the simulations it has been observed that during the formation process there is merging and splitting of diapir structures which change the wavelength.

We demonstrated that the Rayleigh Taylor instability could be a possible mechanism for the formation of the salt-diapiric structures observed in the many parts of the world. The key finding of this thesis is that the diapirs formation is governed by at least three parameters. They are: density contrast, viscosity and layer thickness ratios of salt and sediments.

Maximum kinetic energy ($E_{k,max}$) and onset time of the system ware also found to be a function of above parameters. Viscosity plays an important role in determining the growth rate and dynamics of salt-diapirs

It seems to us that we are still at the primary stage of understanding the dynamics of Salt-diapirs. There is a vast scope of improving our apprehension of convection through laboratory experiments and numerical simulations.

The power law variation for width of diapirs can be examined through enough laboratory experiments. Relation between width of the diapirs and their velocity can be correlated through experiments using PIV or any other techniques.

In literature, very little or no data is available for interpretation of variation in diffusivity with viscosity. Hence, it is imperative to determine this relationship before any actual prediction. Dynamics of the salt-diapirs with step density profiles can be different from those with linear profiles.

Our numerical simulations support the observations from the laboratory experiments. The introduction of strongly non-Newtonian rheology may greatly affect instability parameters such as growth rate and dominant wavelength of perturbations and hence, may alter inter-diapir spacing. Setting top boundary condition as free boundary will be a closer approximation to the air-overlying sedimentation.

References

A. N. B., Poliakov van Balen, R., Podladchikov Yu., Daudre, B., Cloetinghand S., and Talbot C., 1993. Numerical analysis of how sedimentation and redistribution of surficial sediments affects salt diapirism: Tectonophysics, v. 228, p. 199-216.

A. N. B. Poliakov, Y. Podladchikov, C. Talbot – 1993, Initiation of salt diapirs with frictional overburdens:numerical experiments, Tectonics, 228 (3-4),30; 199-210.

B. Daudre, S. Cloetingh**,** 1994**,** Numerical modelling of salt diapirism: influence of the tectonic regime, Tectonophysics, 240(1-4), 59-79.

Chandrasekhar, Subrahmanyan (1981). Hydrodynamic and Hydromagnetic Stability.

C. M. R. Fowler, 2005, Solid earth, an introduction to global physics. Cambridge University Press.

D. A. Nield, 1967, The thermohaline Rayleigh-Jeffreys problem Journal of Fluid Mechanics (1967), 29 : 545-558.

Davies, G. F., 1999 Dynamic Earth: Plates, Plumes and Mantle Convection, Cambridge University Press.

D. R. Moore and N. O. Weiss, Nonlinear penetrative convection, Journal Fluid Mechanics, 61, 553-581.

D. L. Turcotte, 1983, Mechanisms of crustal deformation, Journal of the Geological Society of London, 140(5):701-724.

Francois, A., 1991, Zambia/Zaire Copperbelt notes and materials from field trip, May/June 1991: Unpublished report.

G. Pautot , 1970, Marine Geophysical Researches, Volume 1, Number 1, 61-84.

H. A. Koyi, 2001, Modeling the influence of sinking anhydrite blocks on salt diapirs targeted for hazardous waste disposal, Geology, v. 29(5), 387-390.

Hudec, M. R., and Jackson, M. P. A., 2007, Terra infirma: understanding salt tectonics: Earth-Science Reviews, v. 82, p. 1 24.

I., C., Walton, 1982, Double diffusive convection with large variable gradients, Journal of Fluid Mechanics, 125: 123—135.

John Warren, 2006, Evaporites:Sediments, Resources and Hydrocarbons, Springer 1st edition.

Jackson M. P. A., 1990, Salt diapirs of the Great Kavir, central Iran, Geological Society of America.

Jackson, M. P. A., 1992, Salt dome, in McGraw-Hill encyclopedia of science and technology, 7th ed.: New York, McGraw-Hill, p. 21–24.

Jackson, M. P. A., 1992, Editorial: Expanding frontiers in salt tectonics: Marine and Petroleum Geology, v. 9, p. 330.

Jackson, M. P. A. and Talbot, C. J. (1991) A glossary of salt tectonics. In: Geological Circular 91-4, Bureau of Economic Geology, University of Texas at Austin, USA.

Jackson M. P. A., and J. C. Harrison, 2006 An allochthonous salt canopy on Axel Heiberg Island, Sverdrup Basin, Arctic Canada Geology December, v. 34, p. 1045-1048,

Jackson M. P. A., O. N. Warin, G. M., 2003, Neoproterozoic allochthonous salt tectonics during the Lufilian orogeny in the Katangan Copperbelt, central Africa , Bulletin of the Geological Soc America, 115 (3) , 314-330.

J. S. Turner, 1980, Buoyancy effects in Fluids, Cambridge university press.

K. R. Sreenivas, O. P. Singh and J. Srinivasan ,2009, On the relationship between finger width, velocity, and fluxes in thermohaline convection. Phys. Fluids 21, 026601.

L. L. Nettleton, History of Concepts of Gulf Coast Salt-Dome Formation, AAPG Bulletin,Volume 39 (1955).

M. M. Romer and H. J. Neugebauer, 1991, The salt-dome problem - a multilayered approach, Journal Of Geophysical Research-Solid Earth And Planets 96 (B2) : 2389-2396.

N. A. Haskell, 1937, The Viscosity of the Asthenosphere, , Am. J. Science, Vol. 33, pp. 22–38.

Nalpas, T., and Brun, J. P., 1993, Salt flow and diapirism related to extension at crustal scale: Tectonophysics, v. 228, p. 349-362.

P. G. Baines and A. E. Gill, 1969, On thermohaline convection with linear gradients Journal of Fluid Mechanics, 37:2:289-306.

Polland & Fletcher, 2005, Fundamental of Structural Geology. Cambridge University Press.

Ramberg H.,1980, Diapirism and Gravity Collapse in the Scandinavian Caledonides, Journal of Geological Society, vol. 137 part 3, pp. 261-270.

R. T. Pappalardo and A. C. Barr. The origin of domes on Europa: The role of thermally induced compositional diapirism. L01701, Geophys. Res. Lett., 31, 2004.

R. Weinberger, V. Lyakhovsky, G. Baer, and Z. B. Begin, 2006, Mechanical modeling and InSAR measurements of Mount Sedom uplift, Dead Sea basin: Implications for effective viscosity of rock salt Geochemistry Geophysics Geosystems 7, Q05014, 1-20.

Ryan, W. B. F., Ewing, M., and Ewing, J. I., 1966, Diapirism in the sedimentary basins of the Mediterranean Sea (abstract): Transactions American Geophysical Union, v. 120.

Schenk, P., and M. P. A. Jackson, 1993. Diapirism on Triton: A record of crustal layering and instability, Geology, 21, p. 299-302.

S. D. King, 1995, A numerical journey to the earth's interior, IEEE Computational Science and Engineering, 2(3): 12-23.

S. Balachandar, D. A. Yuen , and D. Reuteler, 1992, Time-Dependent Three-Dimensional Compressible Convection with Depth-Dependent Properties, Geophysical Research Letters, Vol. 19, pp. 2,247–2,250.

S. Mukherjee**,** C. J. Talbot and H. A. Koyi, 2010, Viscosity estimates of salt in the Hormuz and Namakdan salt diapirs, Persian Gulf, Geological Magazine, V14(4), 497-507.

Turcotte & Schubert, 2002, Geodynamics, Cambridge University Press.

Talbot, C. J., 1977: Inclined and asymmetric upward moving gravity structures. Tectonophysics, 42, 159-181.

Vendeville, B. C., and Jackson, M. P. A., 1992, The fall of diapirs during thin-skinned extension: Marine and Petroleum Geology, v. 9, p. 354–371.

Van Keken, P. E., C. J. Spiers, A. P. Van den Berg, and E. J. Muyzert, 1993. The effective viscosity of rocksalt: implementation of steady state creep laws in numerical models of salt diapirism, Tectonophysics, 225, 457-476.

Whitehead, J.A., Luther, D.S., 1975 Dynamics of laboratory diapir and plume models, J. Geophys. Res., 80,705-717.

Weijermars, R., Jackson, M. P. A., and Vendeville, B., 1993, Rheological and tectonic modeling of salt provinces: Tectonophysics, v. 228, p. 143-174.

W. D. Woidt, 1978, Finite-element calculations applied to salt dome analysis, Tectonophysics, 50 : 369 1978.

Web1. http://earthobservatory.nasa.gov/IOTD/view.php?id=6871

Web2. http://oceanexplorer.noaa.gov/gallery/maps/maps.html

Web3. http://www.emeraldgrc.com/assets/images/MC357_L_C5kw1.jpg

Web4.http://www.alumni.gatech.edu/Publications/magazine/win98/earthsci.html

Web5. http://www.glossary.oilfield.slb.com/DisplayImage.cfm?ID=59

Web6. http://nautilus.fis.uc.pt/astro/mirror/solar/eng/earthsp.htm